247-5

(1)

AD 740720

AGARD-AG-161

ACARD-AG-161

AGARD

ADVISORY GROUP FOR AEROSPACE RESEARCH

7 RUE ANCELLE 92 NEUILLY SUR SEINE

AGARDograph No. 161

on

Ablation

by

H.Hurwicz, K.M.Kratsch and J.E.Rogan

DDC
RECEIVED
MAY 2 1972
D

NORTH ATLANTIC TREATY ORGANIZATION

Reproduced by
NATIONAL TECHNICAL
INFORMATION SERVICE
Springfield, Va. 22151

DISTRIBUTION AND AVAILABILITY

NORTH ATLANTIC TREATY ORGANIZATION

ADVISORY GROUP FOR AEROSPACE RESEARCH AND DEVELOPMENT

(ORGANISATION DU TRAITE DE L'ATLANTIQUE NORD)

AGARDograph 161

ABLATION

by

H.Hurwicz, K.M.Kratsch and J.E.Rogan

Edited by

R.E.Wilson

Naval Ordnance Laboratory
White Oak, Silver Spring, Maryland, USA.

DDC
RECEIVED
MAY 2 1977
D

DISTRIBUTION STATEMENT A
Approved for public release;
Distribution Unlimited

This document was prepared at the request of the Fluid Dynamics Panel of AGARD

THE MISSION OF AGARD

The mission of AGARD is to bring together the leading personalities of the NATO nations in the fields of science and technology relating to aerospace for the following purposes:

- Exchanging of scientific and technical information;
- Continuously stimulating advances in the aerospace sciences relevant to strengthening the common defence posture;
- Improving the co-operation among member nations in aerospace research and development;
- Providing scientific and technical advice and assistance to the North Atlantic Military Committee in the field of aerospace research and development;
- Rendering scientific and technical assistance, as requested, to other NATO bodies and to member nations in connection with research and development problems in the aerospace field.
- Providing assistance to member nations for the purpose of increasing their scientific and technical potential;
- Recommending effective ways for the member nations to use their research and development capabilities for the common benefit of the NATO community.

The highest authority within AGARD is the National Delegates Board consisting of officially appointed senior representatives from each Member Nation. The mission of AGARD is carried out through the Panels which are composed for experts appointed by the National Delegates, the Consultant and Exchange Program and the Aerospace Applications Studies Program. The results of AGARD work are reported to the Member Nations and the NATO Authorities through the AGARD series of publications of which this is one.

Participation in AGARD activities is by invitation only and is normally limited to citizens of the NATO nations.

The material in this publication has been reproduced
directly from copy supplied by AGARD or the author

Published March 1972

629.7.023.225

Printed by Technical Editing and Reproduction Ltd

PREFACE

Ablating heat shields have successfully protected many hypersonic vehicles during atmospheric re-entry. Detailed knowledge of the characteristics of many materials and of the interaction mechanisms between materials and high-temperature environments exists. Using this information, very reliable passive heat shields can be designed.

There is an extensive literature containing the results of both analytical and experimental investigations of ablation. Although the technology has reached a mature status, new materials are continually being developed and passive ablating systems are of great interest to heat-shield designers. The well-developed literature and continuing interest in ablation technology make this a particularly suitable subject for an AGARDograph. The intimate coupling between the fluid mechanics of high-temperature boundary layers and ablating materials makes sponsorship by the Fluid Dynamics Panel very appropriate.

This AGARDograph review the advances in ablation technology, the present status, and indicates possible future directions. Ablation analyses are discussed starting with the original simple model in which the amount of material removed is computed from the heat transfer to a non-ablating body and the effective heat of ablation. Analytical methods are carried through the development of the most sophisticated approach which considers the coupling between the boundary layer, the ablating materials, and includes complete non-equilibrium chemistry. The behavior of various materials is compared. The status of today's experimental facilities used to determine ablation behavior is reviewed, including test techniques and instrumentation. Finally, the shape changes and changes in surface roughness which result from ablation are discussed. These changes obviously interact with vehicle performance, flow fields, and aerodynamic characteristics.

The authors have covered, with remarkable completeness, a large complex subject. The bibliography, as well as the material covered here, should be of considerable use to those interested in ablation technology and the design of ablating heat shields.

Dr.R.E.WILSON
Fluid Dynamics Panel Member

The AGARD Fluid Dynamics Panel wishes to thank Dr. Wilson for his contribution in undertaking the review and editing of this AGARDograph.

ABLATION

by

Henryk Hurwicz
Chief Advance Technology Engineer

Kenneth M. Kratsch
Advanced Thermal Protection Systems

James E. Rogan
Branch Chief
Heat and Mass Transfer

Aero/Thermodynamics and Nuclear Effects Department
Research and Development
Advance Systems and Technology
McDonnell Douglas Astronautics Company
5301 Bolsa Avenue
Huntington Beach, California 92647

SUMMARY:

Two decades of advances in ablation technology are reviewed with particular emphasis on developments of the last eight years. Leveling off of research activities is noted reflecting both the space systems requirements and acceptance of ablation as an established means of thermal protection.

Physico-mathematical approaches to analysis of ablation processes are brought out ranging from simplistic heat of ablation concept to the sophisticated analysis of laminar and turbulent flow, non-equilibrium ablation in chemically reacting flow fields including surface reactions and radiative heat transfer. Particular emphasis is given to the synergistic mechanisms occurring during the ablation process. Examples of nosetip interaction with aero/thermodynamic environment at the surface and in depth phenomena is given, as well as striation phenomena on the afterbody are discussed.

Graphite is used as an example of synergistic ablation phenomena and effects because of the interest noted in the literature and because other materials may be treated in a similar fashion. Graphite erosion mechanisms and its microstructure characterization are reviewed. The effects of fillers, binders, porosity, and other parameters are discussed as well as the synergistic effects of the above parameters are also approached in a novel fashion.

Material property and environmental effects on material performance are also reviewed as well as the test simulation requirements. Requirements for further studies of mechanical erosion, other synergistic effects, and extension of facilities range of performance are also noted.

LIST OF SYMBOLS

C_H	Local (dimensionless) pure convective heat transfer coefficient or Stanton numbers including dissociation, mass injection and surface reactions
C_{H_d}	Local (dimensionless) diffusion (mass transfer) Stanton number
C_{H_o}	Local (dimensionless) cold wall heat transfer coefficient or Stanton number uncoupled from species solution
c_i	Specie mass fraction or concentration of ith specie, ρ_i/ρ
C_{p_f}	Specific heat for composite mixture of boundary layer species at constant pressure
C_{p_i}	Specific heat for ith species at constant pressure
C_{p_s}	Specific heat of condensed phase in the decomposing ablator
$\bar{C}_{p_{atmos}}$	Specific heat of mixture of boundary layer species, C_{p_f}
$\bar{C}_{p_g}$	Specific heat for composite mixture of gaseous products of depolymerization at constant pressure

E_{11}	Activation energy used in Arrhenius' rate expression for the representative solid phase resin component ρ_{11}
E_{12}	Activation energy used in Arrhenius' rate expression for the representative completely volatile resin component ρ_{12}
E_2	Activation energy used in Arrhenius' rate expression for the representative completely volatile nylon reinforcement ρ_2
E_{C_3}	Activation energy for Arrhenius' rate expression describing rate limited surface erosion or removal by oxidation of graphite C_3
E_c	Activation energy used in Arrhenius' rate expression describing a form of deposition interaction or coking for the ablation model
f_c	Ratio of char density to virgin plastic density of model ablator
f_f	Number fraction of particles eroded
f_m	Mass fraction of particles
f_s	Solid fraction mechanically eroded
f_l	Melt or evaporation fraction, $\dot{m}_y/\dot{m}_w$, giving the ratio of the rate of evaporation to the total ablation rate in the liquid layer equation
F	External radiation potential from "gloving" internal ablation reactions as a result of char transparency
$g(\eta)$	Reduced (dimensionless) total enthalpy function, refers to I/I_e in the laminar boundary layer solutions
$g_f(\eta)$	Reduced (dimensionless) total "sensible" enthalpy function, $I_f/(I_f)_e$ in the laminar boundary layer solutions
h	Enthalpy function defined as $\sum_i C_i \left(\int_o^T C_i dt + h_i^o\right)$
h_f	Sensible enthalpy function defined as $\sum_i C_i \int_o^T C_{p_i}\, dt$
h_i	Specie enthalpy function, $\int_o^T C_{p_i}\, dt + h_i^o$
h_i^o	Chemical enthalpy of formation of the ith species
h_v	Combined heat of melting and vaporization (also includes combustion and internal reaction effects if not otherwise accounted for) in the liquid layer expression
h_w	Wall enthalpy (at ablator-boundary layer interface)
H	Lumped enthalpy of mass transfer and vaporization or sublimation term
H_e	Total enthalpy at boundary layer edge, same as I_e
I	Total enthalpy function defined as $\sum_i C_i \left(\int_o^t C_{p_i}\, dt + h_i^o\right) + u^2/2$
I_f	Total "sensible" enthalpy function defined as $\sum_i C_i \int_o^t C_{p_i}\, dt + u^2/2$

J	Variable in the "glowing" expression
k	Frequency factor used in Arrhenius' rate expression Also exponent of γ_o to signify two dimensional (K=o) or axi-symmetrical (k=1) Also volume fraction
k_{11}	Frequency coefficient used in Arrhenius' rate expression for the representative solid phase resin component ρ_{11}
k_{12}	Frequency coefficient used in Arrhenius' rate expression for the representative completely volatile resin component ρ_{12}
k_2	Frequency coefficient used in Arrhenius' rate expression for the representative completely volatile nylon reinforcement ρ_2
k_c	Frequency coefficient used in Arrhenius' rate expression describing a form of deposition interaction or coking for the ablation model
$\ldots_e$	Mass fraction of oxygen at the outer edge of the boundary layer
B	Binder mass fraction
$\dot{m}$	Geometric mean mass flux
$\dot{m}_{C_3}$	Mass flux due to surface erosion or removal by oxidation of graphite C_3 when in the rate limited temperature regime
$\dot{m}_{c_s}$, $\dot{m}_s$	Mass flux due to solid surface erosion
$\dot{m}_g$, $\dot{m}_{g_s}$	Composite mass flux of gaseous products of decomposition
$\dot{m}_k$	Mass flux of ablation gas products, includes both $\dot{m}_{k'}$ and $\dot{m}_{k''}$
$\dot{m}_{k'}$	Mass flux of solid species of surface material
$\dot{m}_{k''}$	Mass flux of indepth pyrolysis gas species
$\dot{m}_w$	Total injected mass flux from the ablating surface
$\dot{m}_r$	Mass flux due to mechanical erosion (liquid or solid)
$\bar{M}_{BL}$	Mean molecular weight of boundary layer species
$\bar{M}_{inj}$	Mean molecular weight of injected species
$\bar{M}_O$	Molecular weight of atomic oxygen
$\bar{M}_{O_2}$	Molecular weight of molecular oxygen
n_1	Pressure exponent appearing in rate law expression
n_{11}	Reaction order exponent used in rate law expression for the representative solid phase resin component ρ_{11}
n_{12}	Reaction order exponent used in rate law expression for the representative completely volatile resin component ρ_{12}

n_2	Reaction order exponent used in rate law expression for the representative completely volatile nylon reinforcement ρ_2. Also reaction order exponent for oxidation of graphite by O in rate law expression
n_3	Reaction order exponent for oxidation of graphite by O_2 in rate law expression
n_c	Local partial pressure of char deposition exponent in coking rate law expression
n_c'	Reaction order exponent for a rate law expression describing a form of deposition for the ablation model
p	Local pressure
p_c	Local partial pressure of coking char material
p_e	Local boundary layer edge pressure
p^*	Generalized pressure
P	Molecular Prandtl Number
P_T	Eddy (turbulent) Prandtl Number
$\dot{q}_{blocking}$	Heat transfer rate contribution due to "heat blockage" by mass transfer
$\dot{q}_{chemical}$	Heat transfer rate contribution due to chemical reactions in surface energy balance equation
$\dot{q}_o$	Cold wall pure convective heat transfer rate evaluated by Eckert's reference enthalpy method. Also stagnation point heat transfer rate
$\dot{q}_{or}$	Radiative plus convective heat transfer rate
$\dot{q}_r$	Net radiative heat transfer rate into surface $\dot{q}_{rr}-q^R$ or $-\varepsilon_w \sigma T_w^4 + \alpha_w \dot{q}_{rad}$
$\dot{q}_{rad}$	Radiative heat flux to surface from environment
$\dot{q}_s$	Net heat transfer rate or flux through surface to the interior of ablator $= -(\kappa\, dt/dy)_w$
$\dot{q}_w$	Aerodynamic heat transfer rate to the surface of the ablator from the boundary layer
r	Recovery factor, $= P^{1/2}$ (for lam. B.L.), $= P^{1/3}$ (for turb. B.L.)
R	Universal gas constant
R_o	Reflectivity of the char at the surface of the ablator appearing in "glowing" term
R_y	Reflectivity of the char material in depth at location of evaluation of dF/dy appearing in "glowing" term
$\dot{s}$	Steady state recession rate
t	Time

t_b	Binder bridge thickness
T	Local temperature
T_w	Local "wall" or surface temperature
u	Streamwise component of flow field velocity vector v parallel to s direction
v	Transverse component of flow field velocity vector $\vec{v}$ normal to s direction and parallel to y direction
w_i	Annihilation or creation of species (i.e., mass rate of change of specie) through chemical reactions within the boundary layer
y	Spacial curvilinear coordinate normal to s coordinate and transverse to ablator surface, also depth into material
z	Transformed depth into material (Eq 47)
α	Absorptance in depth used in "glowing" expression. Also viscous resistance coefficient
α_w	Absorptance of surface of the ablator
β^*	Laminar and turbulent boundary layer mass injection parameter
γ	Specific heat ratio, C_p/C_i, for ideal gas; also given as the char mass fraction of pyrolyzing material
Γ	Volume fraction of a degradation polymer in a virgin ablator composite (represented as Phenolic Nylon for the ablator model)
δ_c	Char depth measured from the outer surface of an ablation test model
Δb	Ablator nodal thickness used in transient heat conduction solution
ΔE_c	Energy released by combustion reactions between the gaseous surface material, pyrolysis products and environment combined into one term
ΔH	Boundary layer enthalpy potential for the free stream gas
ΔH_c	Enthalpy of deposition
ΔH_{dp}	Enthalpy of depolymerization and pyrolysis
ΔH_{D_i}	Energy absorbed by pyrolysis
ΔQ	Net energy of decomposition plus sensible enthalpy with original temperature and state as reference
ϵ	Porosity
ϵ_w	Ablator surface emissivity
λ	Parameter defined by Eq 38
η	Similarity transformed (Lee's Dorodnitsyn) or reduced body coordinate y used in laminar boundary layer solutions, also transpiration coefficient used in liquid layer equation
μ	Viscosity
κ	Molecular (for gas species) thermal conductivity
κ_T	Eddy (turbulent) thermal conductivity
ξ	Parameter defined by Eq 39
ρ	Local composite density of all species (gaseous-both boundary layer and pyrolysis products)
ρ_{11}	Instantaneous condensed phase density of the representative solid phase resin component of the model ablator

ρ_{12}	Instantaneous condensed phase density of the representative depolymerized and completely volatile resin component of the model ablator
ρ_2	Instantaneous condensed phase density of the representative depolymerized and completely volatile nylon reinforcement component of the model ablator
ρ_c	Instantaneous condensed phase density due to a form of deposition
ρ_{dp}	Instantaneous weighted sum of local polymer condensed phase densities (ρ_{11}, ρ_{12}, ρ_2)
ρ_i	Density of the ith species in the boundary layer of the same unit volume as ρ
ρ_o	Density of original ablative material before decomposition
ρ_s	Total instantaneous condensed phase densities of local polymer and deposition contributions
$(\rho v)_{rp}$	Mass flux of pyrolysis gases
$(\rho v)_w$	Total ablation mass flux
σ	Stefan-Boltzmann constant
σ'	Eroded surface depth
τ_w	Aerodynamic shear stress

Subscripts

b	Binder
e	Denotes boundary layer edge value. Also end effect region properties
f	Denotes sensible enthalpy term
i	Denotes ith species, initial value; or ith nodal laminar
k'	Denotes ablator char solid phase species
k"	Denotes ablator pyrolysis gas species
j, k, l	Refers to orthogonal rectangular coordinates (3 dim.)
o	Refers to stagnation point value or virgin material
r	Denotes recovery value
r_p	Pyrolysis product
s	Denotes condensed phase; or net surface value
th	Thermochemical
v	Pore volume
w	Denotes "wall" or ablator surface value
∞	Denotes free stream value. Also thick sample properties

1.0 INTRODUCTION

As the scientific/engineering community applauded the success of the early unmanned and manned reentry flights, it recognized the emergence of ablation as a reliable means of thermal protection. These successes intensified the research efforts, which over a decade and a half have advanced the analytical tools from the relatively simple "heat of ablation" approach (1) to sophisticated computer codes which allow a detailed description of the ablation processes (2,3,4,5). Parallel with the analytical developments were the material formulations required to satisfy the more specialized and usually more stringent mission requirements. These combinations produced a new challenge. It was no longer sufficient to be able to predict the gross behavior of ablation materials. It was now required to understand the microscopic behavior in order to adequately give direction to the new materials development required to satisfy the ever increasing system demand. Furthermore, the efficiency of the very process of ablation (removal of mass by thermochemical or thermomechanical processes) had to be maximized and in the limit reduced to perhaps just the surface oxidation as in the case of graphites in some environments.

The purpose of this AGARDograph is to review the advances in- and the status of- the ablation technology after nearly two decades of its application to various space reentry and propulsive systems. Many review papers (with extensive bibliographies) have been published during this period (6, 7, 8, 9, 10, 11, 12) each with somewhat different emphasis on various aspects of ablative phenomena. Some of the reviews stressed ablation mechanisms or material behavior, while others treated environment interaction with ablative system and experimental simulation of ablation phenomena in flight. In the latter part of the sixties production of review papers nearly matched the publication of papers treating new aspects of ablation phenomena. This indicates a leveling off of research activities which may be due to satisfactory solution of engineering problems associated with present or presently contemplated space missions - or in other words attainment of maturity by ablation which now has become an established means of thermal protection and found its way into handbooks. This need not necessarily mean a halt in research and development activities, but it does orient such activities towards specific mission requirements rather than broad theoretical studies so typical of the fifties and early sixties. This decreased emphasis on ablation research per se may be caused by the fact that advanced missions in many cases operate either in environments which invite study of non-receding protection systems or demand reuse of the surface with minimum of refurbishment. The attractiveness of graphites or low density polymerics cannot be underestimated and thus studies of "near" ablation phenomena take precedence over ablation. Still, ablation is one of the most effective and economic means of protection of reentry vehicles. A previous AGARDograph (8) review of the related subject of aero/thermochemistry of ablation by one of the authors of this publication carried the advances in ablation into the sixties and will be treated here as a departing point to avoid repetition. Also the authors have contributed two chapters (13, 14) on the subjects of ablation and thermal protection systems, respectively, which will be used here where required. Driven by requirements of various space missions briefly noted above, the developments, scant that they have been in the last five years, concentrated in the following areas:

1. Internal pyrolysis phenomena for low density ablators.

2. Behavior of graphites in high pressure and temperature environments including internal pyrolysis and mechanical erosion.

3. Empirical evaluation of mechanical erosion of ablators and analysis of shape changes due to thermochemical/thermomechanical forces.

4. Response of materials in environment with high radiative fluxes, and including presence of massive ablation.

5. Better understanding of surface and boundary layer chemistry.

6. Analysis of various synergistic mechanisms including attempts on treatment of coupled reacting boundary layers with radiative heat transfer, non-equilibrium ablation, and surface and flow field chemistry for laminar and turbulent flow.

7. Design and operation of improved arc facilities capable of very high pressures (~200 atm) and/or radiative heat fluxes in combination with previously attained high enthalpy plasmas.

The discussion of the environment per se is out of the scope of this paper. The reader is referred to (15, 16) for such review. However, the interaction of environment with material response and vehicle performance is critical in evaluation of ablation phenomena and as such will be reviewed here. It is hoped that this AGARDograph with its review of the state-of-the-art in ablation analysis, materials behavior testing, and study of synergistic mechanisms will be of help to the scientist and engineer studying and designing space vehicles and developing materials used for thermal protection.

Further work in extending the understanding of synergistic phenomena, mechanical erosion and extending the range of experimental simulation facilities is still in order, as the state-of-the-art is still not sufficient for some of the future interplanetary missions which may be contemplated.

2.0 ABLATION ANALYSES

2.1 General Considerations

The environmental parameters associated with hypervelocity flight in planetary atmospheres affecting ablation mechanisms are: gas temperature, enthalpy, mode of energy transport, total heat load, peak heating rate, shape of the heat pulse, duration of the pulse, external and internal pressure forces, aerodynamic shear, particle impingement, mechanical and acoustical vibration, inertial and dynamic forces, and the chemical reactivity (17). Of primary concern is the means of accommodating the energy converted to heat; i.e., the thermal protection system. This is accomplished in three ways: (a) absorption,

(b) radiation, and (c) reduction of the aerodynamic heat prior to it reaching the vehicle (18).

The requirement to minimize body weight has often led to the choice of materials purposely designed to undergo internal endothermic reactions leading to the formation of a carbonaceous char when heated and to vaporize at the surface exposed to the hypersonic environment. The energy absorption associated with such processes, together with the reduction of the heat transfer coefficient as a result of injection of the products of degradation and the vaporized species into the boundary layer have proved to be extremely effective in providing reliable thermal protection systems (19).

It has been found necessary (20) for efficient design to have an accurate mathematical description of the complex heat and mass transfer phenomena associated with such processes inside the material and an efficient numerical procedure for implementing these calculations based on the mathematical model. In practice, the ablation phenomena are most often encountered in situations where the environmental parameters are nonlinear functions of time. This fact, coupled with the heat shield physically being of finite thickness makes it necessary to perform transient rather than steady state calculations (19). The fully transient solution includes the decomposition in depth with the attendant density and temperature gradients, internal transpiration and radiation generation, material redeposition, source terms for convective and/or radiative input, and provides for a variety of boundary conditions or surface phenomena (20). With the aid of present day computers the solution is practical even for quite complex systems.

It has been shown (19, 21, 22) that an intricate relation between the environment and material response indeed exists and that the solution of the problem must account for them.

Although the transient problem can be solved with a certain degree of reliability for certain combinations of environment and materials, or for steady state experiments, a steady state solution is deemed adequate and is less expensive in terms of computing time. Often, in preliminary design phases, a combination of transient and steady state solutions is used because the costs associated with a comprehensive transient analysis cannot be justified.

One such condition where a steady state analysis (i.e., neglecting indepth phenomena) can be effectively utilized is in the investigation of the ablation requirements for lifting vehicles which enter from orbit and sustain long constant altitude trajectories and minimal decelerations. Here the ablative process remains in the diffusion-limited regime and involves the least intricate of mechanisms. In low heating environments (i.e., heat fluxes less than 75 Btu/ft^2-sec), the surface recession has been shown experimentally to be insignificant. The formation of the char and the influence of pyrolysis on material properties may also be considered inconsequential with respect to a material insulating capability. An assumption of this nature inherently postulates an energy balance of the contradicting effects of pyrolysis whereby blockage of heat transfer by gaseous mass flux is compensated for by neglecting the increase of thermal conductivity due to char formation. Hence, based on these premises in low heating environments, a simplified steady state model may be utilized for estimating ablation requirements. Other conditions where similar approaches can be taken to reduce the problem to a steady state solution are discussed in (20, 23, 24).

2.2 Surface Mechanisms - Transient Ablation

The several energy transfer mechanisms between the boundary layer gas and the ablating surface are shown in Figure 1. The energy balance at the surface extablishes the boundary condition for solution of the boundary layer equations. The energy balance yields,

$$\dot{q}_s = -\dot{q}_w - \dot{m}_w h_w + \sum_{k'} (\dot{m}_{k'})_w (h_{k'})_w + \sum_{k''} (\dot{m}_{k''})_w (h_{k''})_w - \varepsilon_w \sigma T_w^4 + \alpha_w \dot{q}_{rad} - \dot{m}_r h_{c_s} \tag{1}$$

where the mass balance across the surface is given by,

$$\dot{m}_w + \dot{m}_r = \dot{m}_{c_s} + \dot{m}_{g_s} \tag{2}$$

with

$$\dot{m}_{c_s} = \sum_{k'} (\dot{m}_{k'})_w \quad ; \quad h_{c_s} = \frac{1}{\dot{m}_{c_s}} \sum_{k'} (\dot{m}_{k'})_w (h_{k'})_w$$

and

$$\dot{m}_{g_s} = \sum_{k''} (\dot{m}_{k''})_w \quad ; \quad h_{g_s} = \frac{1}{\dot{m}_{g_s}} \sum_{k''} (\dot{m}_{k''})_w (h_{k''})_w$$

The dependency of both C_H and C_{H_d} on $\dot{m}_w$ and implicitly on h_w is seen in the boundary layer expressions. For the surface energy balance it is expedient to define,

$$g^* = \frac{\dot{m}_w}{\rho_e u_e C_{H_d}} \tag{3}$$

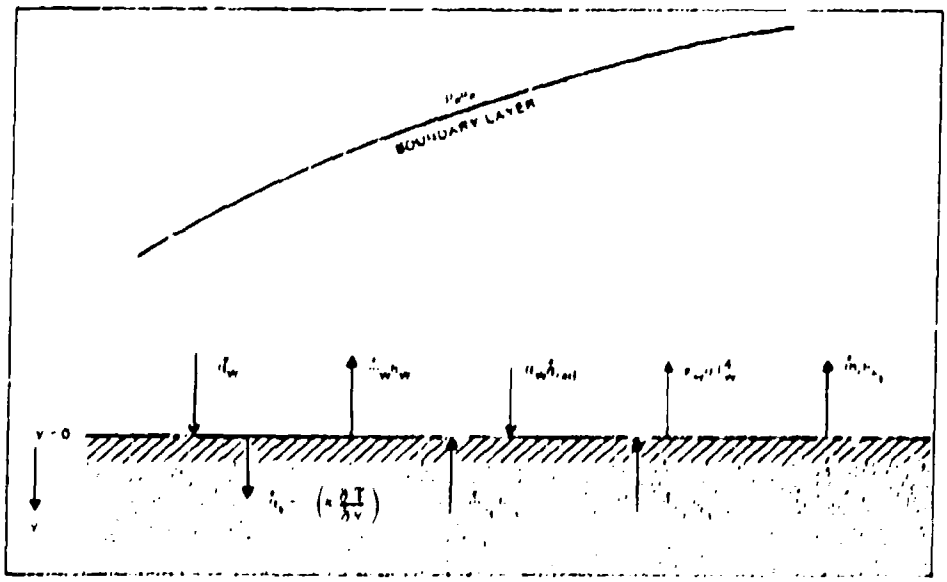

Figure 1. Surface Energy Balance Mechanisms

Substituting for $-\dot{q}_w$ from the boundary layer expressions, one observes,

$$\dot{q}_s = \rho_e u_e C_H \overbrace{\left[(I_f)_r - (h_f)_w\right] + \rho_e u_e C_H \left(\frac{C_H^d}{C_H}\right)\left[\sum_i h_i^o \left[(C_i)_e - (C_i)_w\right]\right]}^{-\dot{q}_w}$$

Surface conduction term

Convection sensible energy transfer with C_H dependent on $\dot{m}_w$

Chemical energy transfer associated with surface reactions from mass transfer

$$+ \sum_{k'} \beta^* \frac{(\dot{m}_{k'})_w}{\dot{m}_w} (h_{k'})_w + \sum_{k''} \beta^* \frac{(\dot{m}_{k''})_w}{\dot{m}_w} (h_{k''})_w \qquad (4)$$

Energy transfer to the surface by condensed material

Energy transfer to the surface by internal gas products

$$- \beta^* h_w j) \qquad - \epsilon_w \sigma T_w^4 \qquad + \alpha_w \dot{q}_{rad} \qquad - \dot{m}_r h_s$$

Energy transfer away from surface by normal gas mass flow

Reradiation

Absorption of incident radiation

Energy transfer by mechanical erosion

The above equation includes the effect of a non-unity Lewis number and is applicable for both laminar and turbulent flow. The energy balance couples the boundary layer solution, which is required to obtain species concentrations and the transfer coefficients, to the indepth solutions of the charring ablator analysis.

Eq (4) is general although, as presented, thermochemical equilibrium is assumed in the boundary layer and at the ablating surface. However, surface mass [illegible]lation rate, $\dot{m}_{c_s}$ can be reaction rate controlled by reactions betw[illegible] the condensed ablator char reactants and the boundary layer species. At low surface temperatures re[illegible] are often rate controlled and $(\dot{m}_{c_s} - \dot{m}_r)$ is determined from an Arrhenius rate expression. At higher temperatures [illegible] rate of injection of $\dot{m}_w$ into the boundary layer can be controlled solely by the diffusion rate of the boundary layer reactants to the reacting ablator surface. In that case, boundary layer solutions must be determined with thermochemical equilibrium reactions involving the surface mass balance species. Gaseous ablation products are determined through the simultaneous solution of (a) all surface thermochemical equilibrium reactions expressed in terms of partial pressures and equilibrium constants; (b) equations of conservation of elemental species at the surface; and (c) Daltons partial pressure law.

The equations for conservation of elemental species come directly from the conservation of specie equations and the catalytic surface reaction boundary condition (15, 25). Fick's law must be assumed in order to demonstrate the same solution form in the turbulent case (21). However, at all times the boundary layer reactants are assumed to be undergoing simultaneous equilibrium dissociation-recombination reactions among themselves at the surface. In fact, a continuum between the two extremes of diffusion limited and rate limited reactions may be effected as long as the processes are confined to the surface. Therefore, reactions between some ablator species and the boundary reactants may be diffusion-limited while others are simultaneously rate-limited (8, 21, 26).

The ablation mechanisms variously termed sublimation, vaporization and/or melting with spallation are characteristically represented as change phase reactions with energy absorption. The sublimation or vaporization is generally associated with the chemical reactions between ambient boundary layer constituents, pyrolysis gases and the subliming surface material. Consequently, the heats of phase change are most often included with chemical enthalpies of formation of the surface char condensed phase species. These phase change reactions effectively decrease the chemical reaction enthalpies.

The ablation mechanism termed mechanical erosion includes liquid layer flow, mechanical spallation, and mechanical shear of surface material. Liquid layer ablation is discussed in the next subsection. Mechanical spallation of charring ablators can be caused by the internal pressure of the gases percolating through the char (27). The stresses can exceed the tensile strength of the char for many low char strength ablators. As a consequence, a part or most of the char can separate from the virgin material. Mechanical shear ablation is characterized by small solid char particles leaving the surface due to surface shear forces. Both of these processes can be expedited by the impingement of small solid particles in the boundary layer as frequently occurs in the rocket nozzle erosion. Mechanical shear ablation is normally associated with more severe environmental conditions and thinner char layers.

Eq (4) is not readily recognizable in the form as presented but can be rearranged to an alternate form. An alternate choice for the surface energy balance is the following expression (19, 26):

$$\dot{q}_s = \underbrace{C_{H_o}\rho_e u_e\left[(I_f)_r - (h_f)_v\right]}_{\dot{q}_o} - \epsilon_v\sigma T_v^4 + \alpha_v\dot{q}_{rad} + \underbrace{\dot{q}_{chemical} + \dot{m}_s H - \dot{m}_r h_o}_{} + \underbrace{\dot{q}_{blocking}}_{} \qquad (5)$$

Pure convection term with C_{H_o} bearing no dependence on $\dot{m}_h$ or h_v

Mass transfer, vaporization and surface chemistry term

blocking term

where

$$\dot{q}_{chemical} = C_{H_d}\rho_e u_e\left(\sum_{i\neq k} h_i^o\left[(C_i)_e - (1+\beta^*)(C_i)_v\right] + \sum_k h_k^o\left(\frac{(\dot{r}_k)_v}{\dot{m}_v}\beta^* - (1+\beta^*)(C_k)_v\right)\right)$$

and

$$\dot{m}_s H = \sum_{k'}(\dot{m}_{k'})_v(h_{k'f})_v + \sum_{k''}(\dot{m}_{k''})_v(h_{k''f})_v \qquad (6)$$

$$\dot{q}_{blocking} = \gamma_2(\dot{m}_{o_s} + \dot{m}_{g_s})\left[(I_f)_r - (h_f)_v\right]$$

where

$$\dot{m}_{o_s} = \sum_{k'}(\dot{m}_{k'})_v \quad ; \quad \dot{m}_{g_s} = \sum_{k''}(\dot{m}_{k''})_v \quad ; \quad \text{and} \quad \dot{m}_v = \dot{m}_{o_s} + \dot{m}_{g_s} - \dot{m}_r \qquad (7)$$

with

$$\gamma_2 = f\left(\left(\frac{\overline{C}_{p_s}}{\overline{C}_{p_{atmos}}} \text{ or } \frac{\overline{M}_s}{\overline{M}_{atmos}}\right)\frac{(\dot{m}_{o_s} + \dot{m}_{g_s})}{\rho_e u_e C_{H_o}}\right)$$

The blocking term arises from expressing $\dot{q}_o$ in terms of C_{H_o} instead of C_H. Where C_{H_o} is the Stanton number, C_H, with zero mass injection (i.e., $\dot{m}_v = 0$). This relieves the responsibility of determining the pure convective Stanton number from solutions to species coupled conservation equations. Empirical relations frequently facilitate determination of the blocking term.

In most cases ϵ_v, σ, and α_v are constants while $\dot{q}_{rad}(t)$ is a table arriving from the shock layer solutions. As stated earlier, quite frequently $\dot{q}_o$ is evaluated by Eckert's reference enthalpy method for a few simple shapes, both for turbulent and laminar environments (19, 26).

2.3 Ablation with Liquid Layer Formation

This mechanism may be considered as an intermediate process to the ablation with only surface mass transfer and the more complex process involving decomposition in depth. The case of simple melting with the liquid layer instantaneously swept from the surface or total vaporization at the liquid-gas interface for very high viscosity materials may be treated by the methods of the previous section. However, cases of combined melting and evaporation of glassy materials where the liquid layer partially flows around the body and partially evaporates require a more complex model of this mechanism. Exact solutions for the transient state arbitrary heat flux are given in (28, 29, 30) at stagnation as well as around the body for arbitrary velocity and temperature gradient in the liquid layer. This solution is coupled with internal radiation transport in (31) and a review of the problem is given in (32).

For specific results of the liquid layer analysis and bibliography the reader is directed to (28, 29, 30, 31, 24). It should be noted that the methods recommended are applicable to any materials displaying liquid layer flow around the body and not just glassy materials. The importance of the internal temperature distribution is particularly noted because of the strong effect of temperature on viscosity of the liquid layer and thus on ablation rates.

2.4 Indepth Mechanisms

It is in this area that technology has exerted considerable effort to arrive at physically meaningful and reasonably accurate solutions (8, 19, 21, 26, 33).

Actually, the surface equations and the coupled boundary layer solutions merely represent a set of boundary conditions setting the stage for the complex transient parabolic heat conduction equation describing the indepth phenomena, that is,

$$\dot{q}_s = -\left(\kappa \frac{\partial T}{\partial y}\right)_w \tag{8}$$

The usual assumptions constraining the indepth solution are as follows:

1. One continuous equation applies across the entire ablator to include the deposition, porous char, decomposition (or reaction) and virgin material regions.

2. The pyrolyzing material either decomposes completely into gaseous species or leaves partially a solid residue capable of melting or entering into heterogenous reactions at the surface.

3. The mass flux of indepth pyrolysis gaseous products are sensed instantaneously at the surface after deposition and/or decomposition reactions.

4. The pyrolysis gases are always in thermal equilibrium with the porous char.

5. The density of the pyrolysis gases are assumed small in comparison to the density of the condensed solid phase.

6. Pyrolysis gas enthalpies are considered known functions of local temperature and external pressure.

7. The thermal conductivity and specific heat of the solids can be represented as linear functions of the condensed phase density and functions of temperature.

8. The ablation model assumes the one dimensional transient heat and mass flow to be normal to the surface.

9. The velocity dependent terms such as those due to viscous stress, friction, mixing, etc., are neglected in the transient heat conduction solution.

10. The ablating surface will serve as the reference frame for the moving coordinate system.

11. Thermal decomposition and deposition are assumed to follow simple Arrhenius' rate expressions.

12. Internal radiation heat absorption in a semi-transparent silicious char is usually represented as a gradient expression added to the heat transfer equation.

The preceding are generally accepted as the standard assumptions accompanying an indepth ablation solution. However, other options exist presenting internal pressure distribution effects; transpiration cooling; and models for evaluating the internal radiation contributions.

Upon exercising the above assumptions one may obtain directly the following transient indepth reacting heat conduction equation in one dimensional partial differential equation form (21, 34):

$$\underbrace{\rho_s C_{p_s} \frac{\partial T}{\partial t}}_{\text{Sensible energy exchange}} = \underbrace{\frac{\partial}{\partial y}\left(\kappa \frac{\partial T}{\partial y}\right)}_{\text{pure conduction}} + \underbrace{\dot{m}_g \bar{C}_{p_g} \frac{\partial T}{\partial y}}_{\text{Energy exchange due to mass transfer and cracking}} + \underbrace{\dot{s}\, \rho_s \frac{\partial s}{\partial y}}_{\text{Energy exchange due to moving coordinate system}}$$

$$+ \underbrace{\Delta H_{dp} \frac{\partial \rho_{dp}}{\partial t}}_{\text{Energy exchange due to decomposition (i.e., pyrolysis and depolymerization}} + \underbrace{\Delta H_c \frac{\partial \rho_c}{\partial t}}_{\text{Energy exchange due to deposition (i.e., coking)}} + \underbrace{\frac{\partial F}{\partial y}}_{\text{External radiation exchange due to char transparency}} \tag{9}$$

with the auxillary equations

$$\frac{\partial \rho_g}{\partial t} = \frac{\partial \dot{m}_g}{\partial y} \quad \text{and} \quad \rho_{dp} + \rho_c = \rho_s \tag{10}$$

Enthalpy of decomposition, ΔH_{dp}, and enthalpy of deposition, ΔH_c, are $f(P_e, T)$. Typically, an example decomposition reaction might be (3, 35).

$$\underbrace{\Gamma(E_{a_1} R_{b_1} P_{c_1})_{d_1} + (1-\Gamma)(E_{a_2} R_{b_2} P_{c_2})_{d_2}}_{\text{Virgin Composite}} \xrightarrow{\Delta H_{dp}} \underbrace{e(T)R_2 + f(T)ER_4 + g(T)E_2R_2 + l(T)P}_{\text{Pyrolysis gaseous products}} \underbrace{+E_n}_{\text{solid char}} \tag{11}$$

such that $\rho_{dp} = \Gamma(\rho_{11} + \rho_{12}) + (1-\Gamma)\rho_2$ and Γ being the volume fraction where ρ_{12} and ρ_2 are completely converted into gaseous products.

Then the governing Arrhenius rate expression might be, for instance,

$$\frac{\partial \rho_{dp}}{\partial t} = -\left\{ \Gamma k_{11}\rho_{11}(0) \left[\frac{\rho_{11}(t) - \frac{f_c}{\Gamma}\rho_o}{\rho_{11}(0)}\right]^{n_{11}} e^{-\frac{E_{11}}{RT}} + \Gamma k_{12}\rho_{12}(0) \left[\frac{\rho_{12}(t)}{\rho_{12}(0)}\right]^{n_{12}} e^{-\frac{E_{12}}{RT}} + (1-\Gamma)k_2\rho_2(0)\left[\frac{\rho_2(t)}{\rho_2(0)}\right]^{n_2} e^{-\frac{E_2}{RT}} \right\} \tag{12}$$

where $f_c = \frac{\rho_{char}}{\rho_{virgin}}$

Similarly for a typical deposition reaction which might be $2E_2R_2$ (pyrolysis gas) $\xrightarrow{\Delta H_c}$ ER_4 (further pyrolysis gas) + 3E (solid char) the governing Arrhenius rate expression would probably be

$$\frac{\partial \rho_c}{\partial t} = -k_c\rho_c(0)\, e^{-\frac{E_f}{RT}} (\rho_c)^{n_c} \left[\frac{\rho_c(t)}{\rho_c(0)}\right]^{n_c} \tag{13}$$

Note the arrow in the above deposition reaction shows going to completion as stated in the approximations. A reverse reaction would involve equilibrium constants and partial pressure dependence.

Considering this as the complete picture then conservation requires, as seen by the auxiliary equations, that

$$\frac{\partial \dot{m}_g}{\partial y} = \frac{\partial \rho_s}{\partial t} = \frac{\partial \rho_{dp}}{\partial t} + \frac{\partial \rho_c}{\partial t} \tag{14}$$

Finally the char transparency radiation term as proposed in (2) would be quite adequate for this typical analysis, namely

$$\frac{\partial F}{\partial y} = \alpha(J-J_e) + a(1-R_o)F_o \frac{e^{-a(y-\sigma)} + R_o e^{-a(2\lambda-y-\sigma)}}{1-R_o R_y e^{-2A(\lambda-\sigma)}} \tag{15}$$

where J is solved from the auxiliary set of equations

$$\frac{\partial^2 J}{\partial y^2} = a^2(J-J_e) \tag{16}$$

$$\frac{\partial J}{\partial y} = -\frac{a^2 F_1}{\alpha} \tag{17}$$

$$J_e = 4\mu_e^2 \sigma T^4 \tag{18}$$

with boundary conditions $J\ (y=\sigma) = \alpha_W \dot{q}_{rad}$ (19)

and

$$F_1(s) = -\frac{\alpha}{a}\frac{1-R_o}{1+R_o}\alpha_W \dot{q}_{rad} \tag{20}$$

and

$$J(y=\lambda) = F_1(\lambda) = 0 \tag{21}$$

All of these equations are thence assembled in finite difference form and solved numerically on the computer (21, 36). The solutions provide accurate thermal histories and profiles throughout the ablator as well as a realistic prediction of the decomposition and deposition process.

2.5 Mechanical Removal

It is known that some ablation materials under certain external or internal high-pressure conditions may either experience mechanical spallation of the surface or other failures resulting in mechanical removal of material. The mechanisms or failure criteria for such ablation processes have been studied (27, 37), criteria assumed and postulated, and their results incorporated in the thermal ablation models. Further detail will be provided in Section 3.0.

2.6 Specialized Ablation Models

The sample model of ablation material exhibited earlier to represent the typical indepth decomposition and deposition mechanisms was symbolically that of phenolic nylon in absence of mechanical removal. The symbolic pyrolysis gases released by decomposition of this model were a four component mixture, namely ER_4, E_2R_2, R_2, and P representing respectively methane (CH_4), acetylene (C_2H_2), hydrogen (H_2), and a combination of assumed nonparticipating gases (i.e., non-reacting with boundary layer species) such as nitrogen and hydrogen cyanide (35). In this model the completely volatile nylon reinforcement was represented by ρ_2 whereas the ρ_{12} (completely volatile) and ρ_{11} combination represented the density of the phenolic resin with Γ being the volume fraction of phenolic resin in the entire virgin plastic composite (3, 21, 38). The last reference treats a rather sophisticated coupled chemically reacting boundary layer/charring ablator problem with interesting results, but unfortunately not quite tractable by a practicing engineer. With the equilibrium surface reactions between these pyrolysis gaseous products and the boundary layer species in mind, the choice of which components are representative or most significant becomes largely an art depending on the range of surface temperatures (4). The problem of handling consecutive equilibrium surface reactions involves no more than writing one combined stoichiometric expression and the associated effective equilibrium constant. On the other hand, simultaneous equilibrium surface reactions momentarily appearing as primary, secondary and tertiary in some order, only to have their roles reversed or permuted as the temperature changes, presents the only real challenge for choice of original pyrolysis components. This certainly would seem to preclude the four component model from even representing the ablation of phenolic nylon much less the general ablator.

However, knowledge of the thermochemical properties of materials such as teflon or carbon and the graphites and their respective ablation behavior, in such veritable detail permits specialized handling. This greatly simplifies the ablation equations further facilitating inclusion of more detailed chemistry (39). For instance, carbon (graphite) can form the following ablation products limited in the oxidation and sublimation regimes: (4, 40, 41, 42) C, C_2, C_3, C_4, C_5, C_O, C_{O_2}, C_N, and C_2H_2. For quartz the chemistry is much simpler as the only reaction requiring consideration is (24).

$$SiO_2(\ell) \rightleftarrows SiO + \frac{1}{2}O_2$$

where (ℓ) denotes liquid.

Intermediate steps can include:

$$SiO_2(\ell) \rightleftarrows SiO_2$$

$$SiO_2 \rightleftarrows Si + O_2$$

$$SiO_2 \rightleftarrows SiO + \frac{1}{2}O_2$$

For graphite where the surface reactions and hence ablation is reaction rate limited the following heterogenous completion reactions are representative, namely:

$$C\ (s) + O \rightarrow CO$$

Simultaneous completion (reaction rate limited)

$$C\ (s) + \frac{1}{2}\,O_2 \rightarrow CO$$

The mass flux of C (s) leaving the surface by interaction with O and O_2 being represented by the combined rate law and Arrhenius expression:

$$\dot{m}_C = \text{const}\ P_e^{n_1} \left[\frac{\bar{M}_C}{\bar{M}_O}(C_O)_W\right]^{n_2} \left[\frac{\bar{M}_C}{\bar{M}_{O_2}}(C_{O_2})_W\right]^{n_3} \exp^{\frac{E_C}{RT}} \tag{22}$$

Similarly for teflon whose ablation and surface erosion occurs at the surface, the following rate dependent formation of the teflon monomer and a subsequent oxidation reaction can be expressed as (43).

$$\begin{gathered}(C_2F_4)_N(s) \rightarrow N(CF_2)_2(s) \rightleftarrows N(CF_2)_2(g) \rightleftarrows 2N(CF_2)(g) \\ (CF_2)(g) + O \overset{K_{10}}{\rightleftarrows} COF_2\end{gathered} \tag{23}$$

(with arrows in both directions for diffusion limited and forward direction only for rate limited reactions).

The basic advantage of considering the teflon, quartz, and carbon models separately from the generalized model lies in the feature of having to consider only indepth transient heat conduction internally. All reactions are confined to the surface area.

The silicone elastomers conversely pursue the opposite route. Ablation occurs primarily through the indepth decomposition mechanisms with relatively sparse surface erosion reactions. The porous silica char produced provides a highly insulative layer that primarily reradiates energy back to the environmental flow field (44). The basic indepth reactions consist of unzipping of the highly cross-linked bonds of the elastomer with the release of a few basic pyrolysis gases such as water vapor, carbon monoxide and methane (7). A highly porous silica char, SiO_2 may reduce to silica carbide and carbon monoxide later capable of entering into reaction with the boundary layer constituents and forming the dioxide again (7, 45, 46).

The silica-resin composites present the combined complexities of the silicone elastomeric indepth reactions with the phenolic-nylon's phenolic resin decomposition (46) and quartz's surface reaction characteristics (24).

The carbon-graphite resin composites essentially proceed with the same or comparable indepth reaction kinetics as the phenolic nylon model with char erosion surface reactions similar to the pure graphite model (39, 47).

2.7 Strongly Radiating Shock Layers

At entry velocities above 45,000 fps, stagnation point heating can be primarily caused by strong atomic line and continuum radiation. Under these conditions, ablation rates result in mass fluxes from the heat shield on the order of 20 percent of the air flux through the shock (48, 49). Classically, such conditions result in "blown-off" shock layers with the convective heating reduced many orders of magnitude below the value that would occur without blowing.

Since most of the coupling radiation occurs in the ultraviolet spectrum, ablation-products injection will not offer any significant alteration of these phenomena, although they will be somewhat

accentuated. These conclusions were borne out by Coleman, Lefferdo, Hearne, and Vojvodich (48) where radiative coupling to ablating heat shields were studied; reductions in radiative heating from ablation-products injection for the cases considered by Rigdon, Dirling, and Thomas (49) reach 30 percent.

The recent decrease in emphasis on manned entry missions at velocities in excess of 36,000 fps have witnessed a corresponding decrease in the attempts to further understand and analytically model the phenomena.

3.0 SYNERGISTIC ABLATION MECHANISMS

It is known that some ablation materials under certain external or internal high pressure conditions may either experience mechanical spallation of the surface material strata or other failures resulting in mechanical removal of material. The mechanisms or failure criteria for such ablation processes have been studied, (27, 37) criteria assumed and postulated, and their results incorporated in the thermal ablation models. Although these materials have been studied analytically with some vigor, recently developed high pressure test facilities have revealed a large deficiency in analytical predictions of the observed mass-loss data. As a consequence, analysts have resorted to empirical and semi-empirical correlations of the test data with rather questionable results when extrapolated to actual flight environments.

Understandably, empirical correlations of test data are at best provisional; little insight into the actual mechanisms operative during the ablation processes is gained (50, 51). Conversely, rather sophisticated analyses of the thermochemical erosion of a variety of carbon-based materials has evolved (3, 52, 53). Development of these analyses has been closely followed by a number of papers dealing with various aspects of the thermomechanical ablation problem (37, 27, 35) and are specialized to the particular material under study. The composite of these analyses has failed to provide repetitive correlation of the test data -- obviating their generality. It is now evident that a large number of disciplines are required to effectively approach the analytical description of even what previously was described as homogeneous materials; e.g., graphite.

Graphite response mechanisms will be used here as a typical example. Analogous response would occur in some other materials.

3.1 Environmental-Ablation Interaction

3.1.1 Typical Nose Tip Interaction

The definition of material response that is required to account appropriately for the interaction of the local aerodynamic environment at the exposed material surface and for the resulting indepth phenomena is complex. To illustrate this behavior in an applied situation, a nose tip is analyzed for a ballistic entry flight case perturbing first the extent of mechanical erosion and then transition criteria. The results are presented in Figure 2.

The results of the sensitivity analysis for the cases examined are:

Case 1. The basis for the nose shape change results in this flight simulation case is a siliceous nose tip material. A nominal transition criterion neglecting roughness and blowing was employed to determine transition to turbulent heating. Mechanical erosion was deduced from ground test data report in (54).

Case 2. This case shows the sensitivity of mechanical erosion effects on nose shape change (55) and recession. The case is identical to Case 1 with the exception that the mechanical correlation utilized was for a factor of 3 increase greater in recession over that employed with the silaceous material in Case 1 at a stagnation pressure of 100 atm.

Case 3. This case retains all assumptions of mechanical erosion for the silaceous material used in Case 2. The only exception is that laminar flow is assumed to persist throughout the reentry flight.

Case 4. This case employs the same material assumptions as Cases 2 and 3, with the exception that turbulent flow is presumed to exist from the start of reentry throughout the flight period. The all-turbulent run indicated here simulated a fully turbulent stagnation point throughout the flight.

In summary, the results reflected in Figure 2 show large changes in spatial and temporal nose shape configurations due to the thermomechanical erosion assumptions. Extremes in all-laminar and all-turbulent boundary flow produce significant effects upon both the final shape and total tip recession. When using the same mechanical erosion correlation, the nominal transition criteria naturally lie between these two extremes and are more closely represented by an all-turbulent layer. The significance of mechanical erosion and flow field assumptions are clearly evidenced by this illustrative case. For purposes of this paper, primary attention is focused on mechanical erosion and the relatively new approaches used to analyze and gain insight into the mechanisms promoting this erosion.

3.1.2 Afterbody Response

Recently differential ablation patterns have been observed on afterbody surfaces. Previously, intriguing ablation patterns on meteorites and tektites had been noted and studied (e.g., References 56, 57, 58). Later, attention was focused on cross-hatching and related roll torques by the advent of small

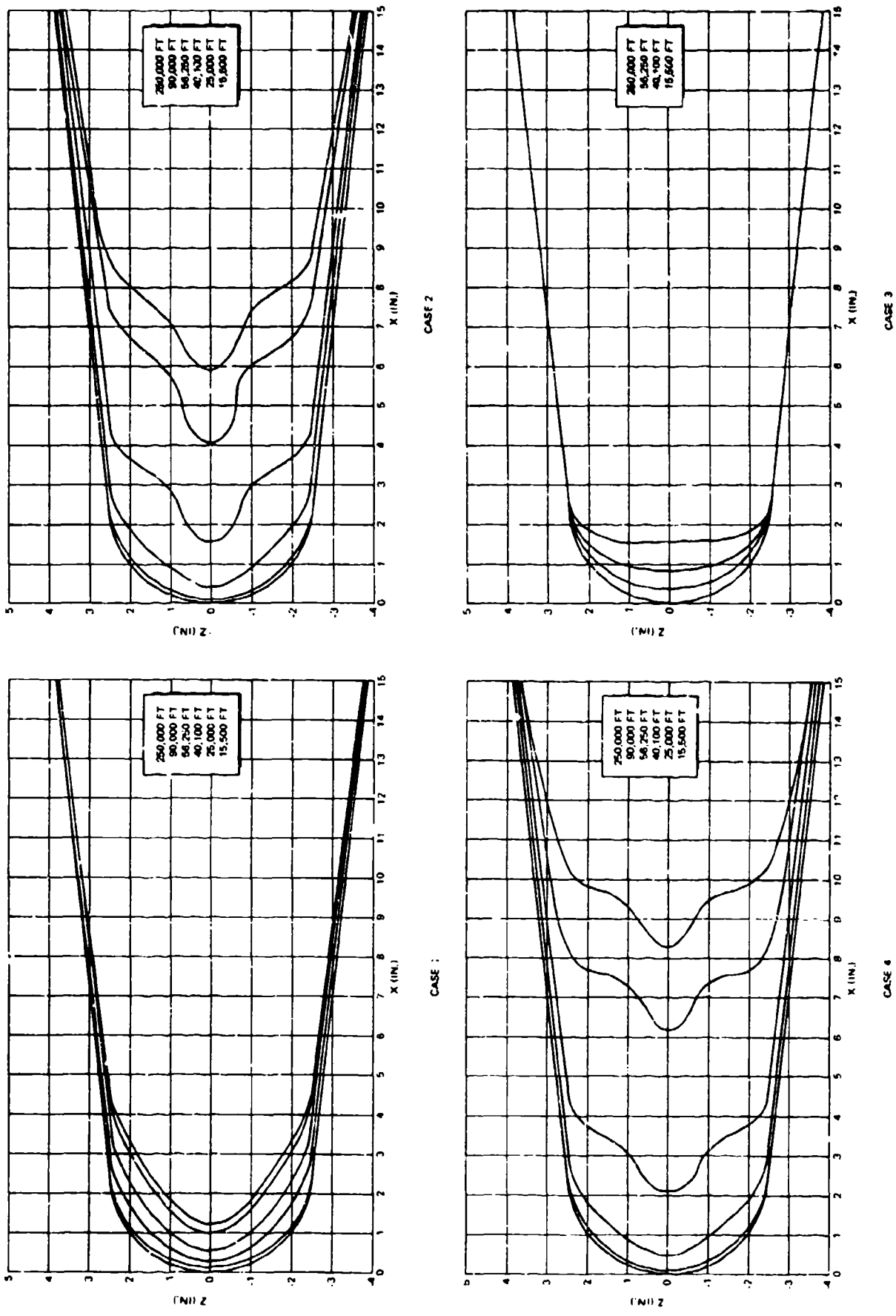

Figure 2. Nosetip Flight Simulation

hypervelocity vehicles and their erratic roll behavior. Larson and Mateer noted the development of cross-hatching on camphor models into a pattern resembling that observed on many meteorites (59). Canning, Wilkins and Tauber have reported on turbulent wedges, streamsite grooves, and cross-hatched patterns from their ballistic range and wind-tunnel tests and proposed a physical flow model to explain these patterns (60, 61, 62).

Laganelli and Nestler have reported the results of tests in the Malta rocket exhaust facility and the Langley 8-ft structures tunnel on a wide variety of materials, ranging from wood to carbon phenolic (63). Particular emphasis was placed on char-forming materials.

Williams (64) (Figure 3) obtained cross-hatching in a hypersonic wind-tunnel on several low temperature ablators, mostly subliming camphor and Korotherm. He showed the scale of cross-hatching decreasing with increasing pressure for camphor and the pattern of melting-vaporizing naphthalene to be similar to that of subliming camphor. A unique feature of these tests was the direct measurement of roll torques during the ablation process. Later tests (65) extended this work to a more realistic simulation of the reentry vehicle flight regime and geometry. Similar results were obtained in camphor and wax by Stock and Ginoux (66). McDevitt (67) investigated the coupling between roll dynamics and ablation patterns by testing spinning Korotherm and ammonium chloride models in a hypersonic wind tunnel.

Reproduced from best available copy.

Figure 3. Cross-hatching on a 20° Camphor Cone at Mach 6

Various analyses have been made to explain the phenomenon of cross-hatching; only a few can be mentioned here. Tobak (68) suggested vortices as the origin of cross-hatching. Nachtsheim (69) believes a thin liquid layer is essential. Probstein, Gold and Scullen (70) believe that cross-hatching occurs because of a resonance between boundary layer disturbances and a suitable inelastic deformable surface. In an investigation of the pressure and temperature distributions over a two-dimensional nonablating wavy wall, Williams and Inger (71) have theoretically proved and experimentally confirmed a wall temperature phasing correspondence to boundary layer pressure disturbances. Williams and Inger (71) also report that a pre-cross-hatched nonablating model confirmed cross-hatching experience by indicating higher heat transfer to the valleys than to the ridges; this is diametrically opposed to normal supersonic heat transfer experience which shows peak heating on protuberances.

3.2 Graphite Erosion Mechanisms

It has been observed by a number of investigators (72, 73, 74), that under certain pressure-temperature environments bulk polycrystalline graphite undergoes loss of solid material of minute quantity characteristic of the constituent size of the material components. In a closer examination of the type of behavior that occurs when graphites are subjected to high-temperature environments, a cross section of a tested specimen is shown in Figure 4. The figure reflects an indepth degradation of material, showing a rather open irregular structure proceeding into the material and the appearance of an interface showing a less porous structure with increased material mass. A view of the surface demonstrates large differences in material structure and preferential loss of material revealing irregular rectangular appearing particles.

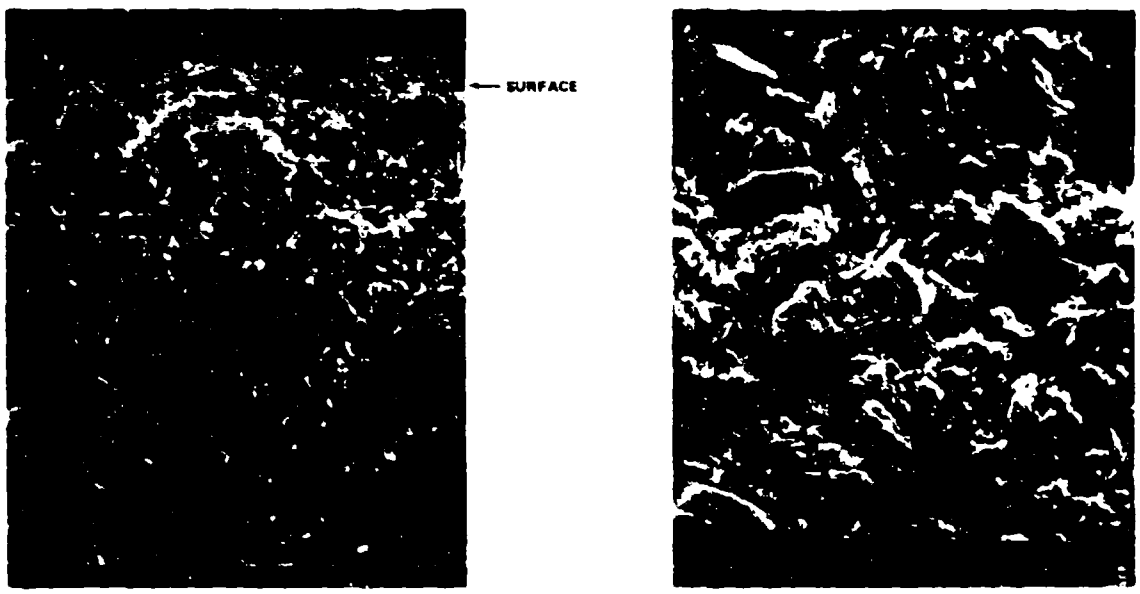

Figure 4. High Temperature Exposed Cross Section and Surface Photomicrograph of Graphite (ATJ-S)

Some perspective can be focused on the results of the ablated pattern illustrated in Figure 4. Graphite, by its very nature, is an inhomogeneous material composite consisting of filler particles and binder structure with a high degree of porosity. The differential nature of the constituent materials used in fabrication of the graphite is believed to result in preferential erosion giving rise to an irregular, roughened surface that interacts closely to the environment at the heated surface of the material. This interaction involves a complex association of the local environment and the material behavior.

3.2.1 Physical Characteristics

An understanding of the microstructure of graphite requires some knowledge of the processes by which graphite is formed. The commercial graphites used in aerospace applications can be described as

synthetic or manufactured. These bulk graphites are manufactured by mixing an organic binder, usually a coal tar pitch, with carbon filler particles and molding or extruding the mixture to form a "green" billet. The binder is then carbonized by heating to temperatures on the order of 1500°F, followed by further heating to temperatures up to 5400°F, to produce a more ordered microstructure. The filler material may be any particulate graphite or carbon, such as natural graphite, carbon black, coke, etc. For economic reasons, filler material is most commonly made from the coked residue of the petroleum refining process. The coke mass is crushed and ground to eliminate gross porosity, and screened into controlled particle sizes. Because of unavoidable intercrystalline micropores, the particles retain a minimum porosity of 5 to 8 percent (75), resulting in apparent densities of about 2.0 to 2.2 gm/cc.

Figure 5 provides a schematic of the proposed bulk graphite arrangement after graphitization (the description given here abets the excellent discussion of graphite by Riley [76]). The filler particles appear as an array of loosely packed irregular-shaped coke elements cemented together by the carbonized binder. The ratio of binder-to-filler weight may be varied over wide limits, with normal practice being between 20 to 40 percent. In the baking cycle (1500°F) the pitch binder is pyrolysed, losing about 40 to 50 percent of its initial weight. During the baking cycle, and upon subsequent graphitization, the binder shrinks. Since shrinkage is constrained by the filler particles, the volume nominally occupied by the binder has a large void content. The resulting macropores in the binder allow for easy passage of evolved gases through the binder matrix and account for the relatively high porosity of bulk graphite. Each filler particle is held in the resulting matrix by a network of binder bridges occasionally interrupted by interconnected macropores. The macropore diameter varies, but is about the same as the diameter of the filler particles. A line of interconnected macropores may propagate a mechanical failure since this is the path of minimum cross section. The microstructure evidenced in Figure 5 exposes the heterogeneous qualities of graphite in detail. Filler particles consist of closely packed crystallites and intercrystalline micropores. Significantly, the crystallites are not completely ordered; the binder crystallites are even less ordered, which accounts for the minimal anisotropy exhibited in the thermophysical properties of bulk graphite.

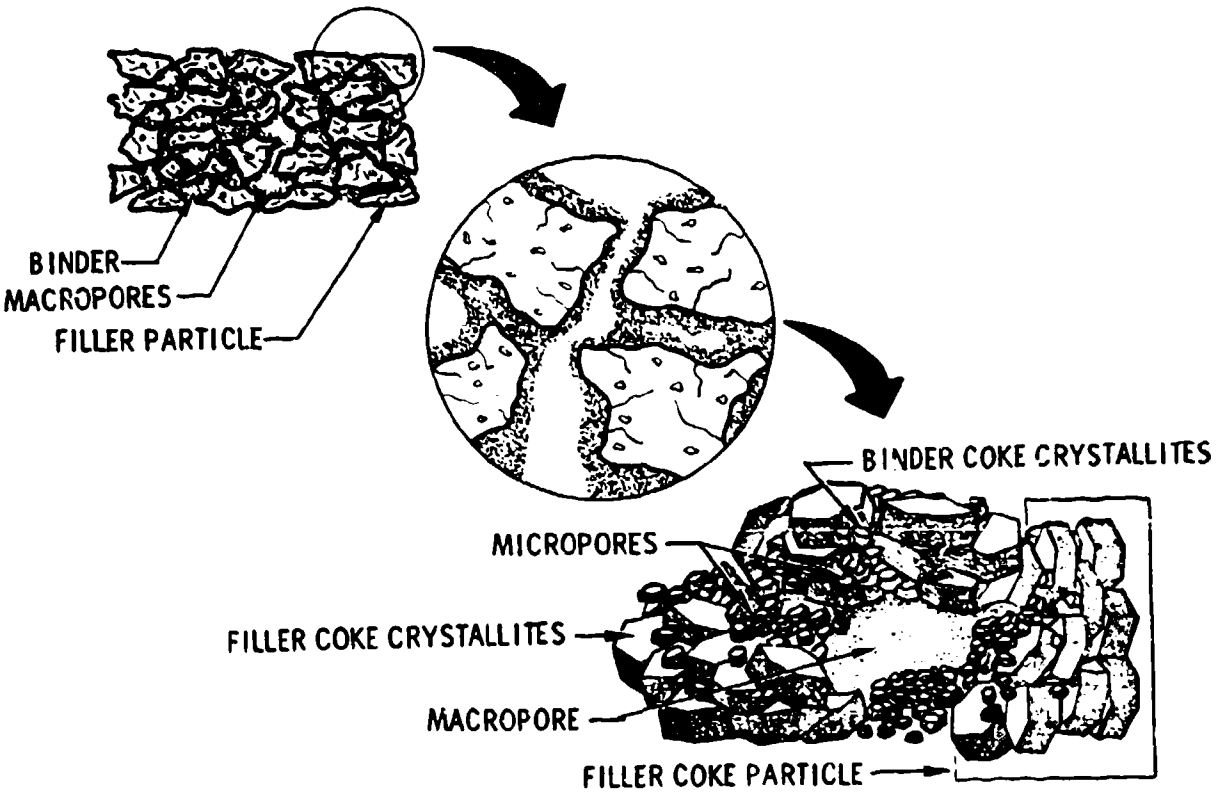

Figure 5. Schematic of Graphite Microstructure

3.2.2 Preferential Erosion

Rather extensive investigations of the preferential er sion aspects of graphite have occurred in recent literature. Maahs and Schryer (72) observed loss of particle solid of graphite nose tip

materials in environments typified by model stagnation pressures of 4 to 5 atm stagnation pressure. More recently, Lundell (73) photographically showed proof of loss of particulate solid graphite in model stagnation pressures as low as 3 atm. These observations have not been confined to air arc testing alone, as evidenced by the observation of Whittaker (74) who observed particulate solid loss and experimentally trapped the evolved solid mass.

Recent experimental and analytical interpretations of the preferential erosion of graphitic materials have been offered by Kratsch (77) and McVey (78). Both addressed the high pressure performance of graphite where large deviations in thermochemical ablation calculation were noted. Typical experimental evidence of the departure from thermochemical erosion given in (77) is shown in Figure 6. Denman (79) reviewed the graphite ablation problem from an environmental approach, calculating shape change and recession rates for smooth and roughened walls. It suffices to state that the composite of these analyses remain semiempirical and provide little insight into the relation of the observed erosion to the material composition.

Behavior of the graphite shown in Figure 4 demonstrates a complex interaction of materials composition and local aerodynamic environment. To identify the material quantities that have an important role in the ablation performance requires a systematic approach to isolation of individual erosion mechanisms. The approach adopted to elucidate erosion mechanisms for graphite materials is schematically represented in Figure 7. The figure represents the compositional structure of graphite when subjected to hyperthermal reentry environments.

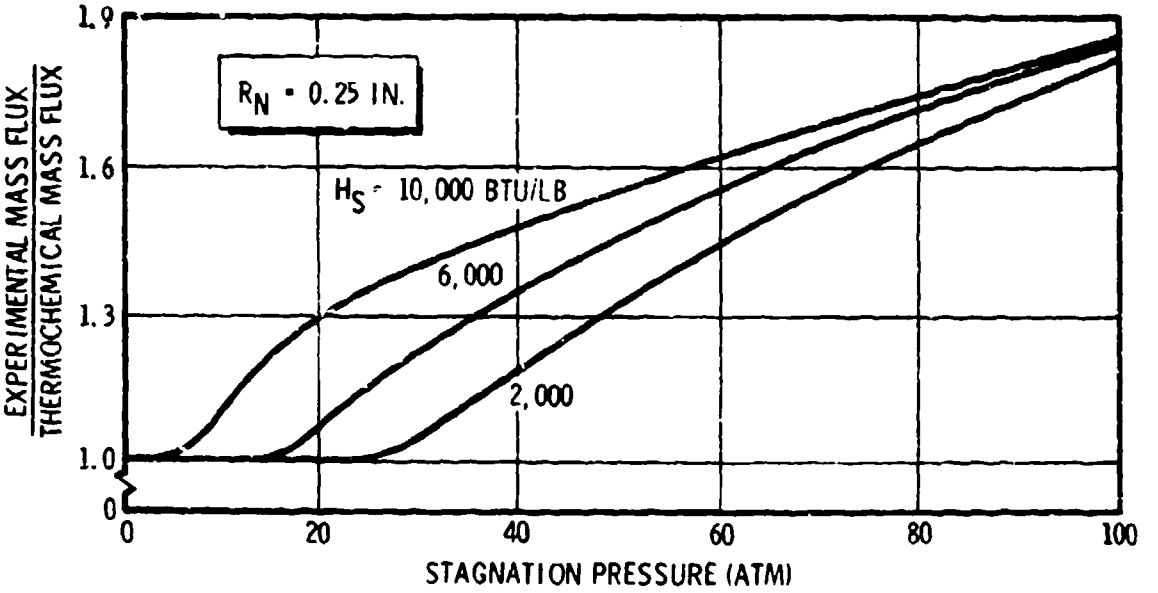

Figure 6. Ratio of Experimental and Thermochemical Mass Fluxes

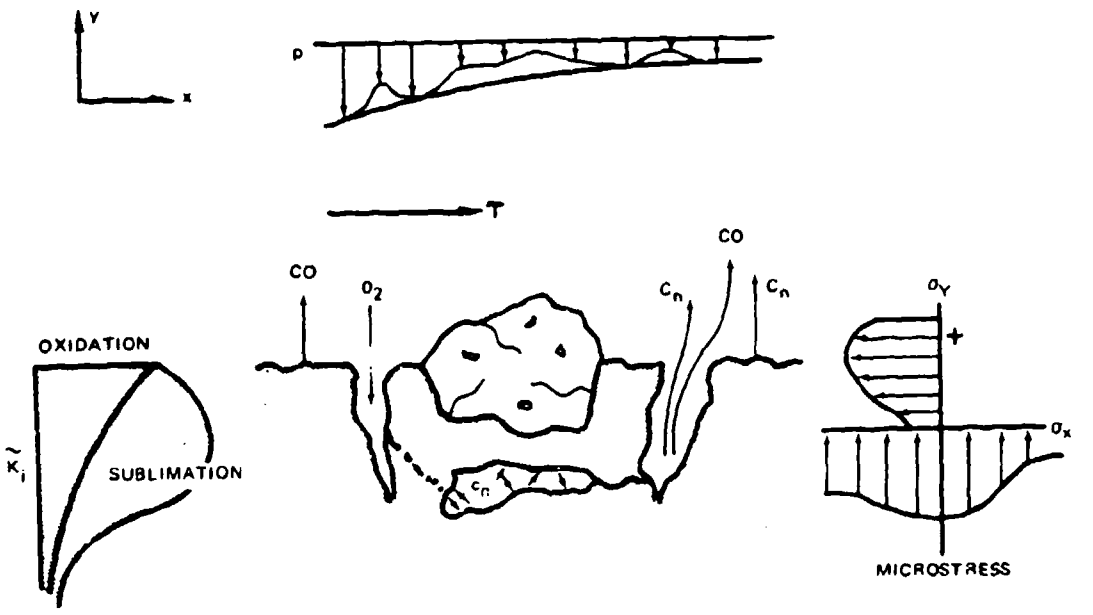

Figure 7. Micromechanical Erosion

In air environments, the boundary layer constituents chemically react with the carbon structure resulting in thermochemical erosion by oxidation and sublimation of the carbon structure. The porosity inherent in graphite affords a means of subsurface chemical erosion to occur. These effects encompass subsurface oxidation and sublimation that are closely related to the material's macro and microporosity. Porosity alone is not confined to that open to attack by the boundary layer constituents but includes closed pores which may, at sufficiently elevated temperatures, act as miniature pressure vessels as sublimation occurs within the enclosed internal pore surface area.

Consequently, the differential microstructure between filler particles and binder material holding the particles, through a labyrinth of binder walls connected and interlaced throughout the pores may have significant effect on the micromechanical erosion observed by graphitic materials. The preferential removal of either binder or filler particle material leads to a differential recession rate causing an irregular surface, promoting surface roughness and increased heat transfer. Material protruding about an aerodynamic surface is subject to aerodynamic shear and pressure forces which, depending on the material strength, extent of exposure, and bonding, may be sufficient to erode solid from the surface. If the material pore structure is small and constricted, a pressure differential may exist across the material causing local failure of the partially eroded material.

To quantize material composition and variables which may be significant in isolating individual erosion mechanisms contributing to the total performance of graphite, necessitates an approach which first dissociates material variables interactions from the applied environment. With the material quantities characterized, such as binder content, filler particle size and distribution, pore distribution and shape, etc., concise statements can be made about the material variables influences in aerodynamic environments. These material variables can then be related to the observed erosion occurring and developmental goals for improved graphitic materials stated.

3.2.3 Surface Roughness Effect on Heat Transfer

The material characteristics are though to directly influence heat transfer to the material ablating surface. Surface roughness elements can occur from material impurities and preferential erosion; or they can be inherent in the material finish, even when highly polished. The effects of surface roughness on heat transfer have been treated by numerous investigators (80 through 93) with varying objectives. The bulk of the reported studies have been concerned either with singular roughness elements (both two- and three-dimensional) on symmetrical bodies or with roughness elements on flat plates. The utility of these data in a high-pressure environment, and as related to heat transfer, has yet to be determined. The data of Bertram, et al. (91, 92, and 93) would appear to be useful in that the effects of the sinusoidal variation can be directly related to some of the irregularities existing on graphite materials. More recently, Welsh (94) and Akin and Marvin (95) have investigated the effects of surface roughness on spherical geometries in representative high-pressure environments. Reference 95 presents results obtained in a combustion-driven shock tube. These results show an anomalous behavior of the convective heat transfer in that the data deviate from the laminar theoretical predictions, increasing directly with increasing stagnation pressure (Figure 8). The deviation from theory is as high as 60 percent. It has been postulated that this deviation is due to the flow being in a transitional state (from laminar to turbulent).

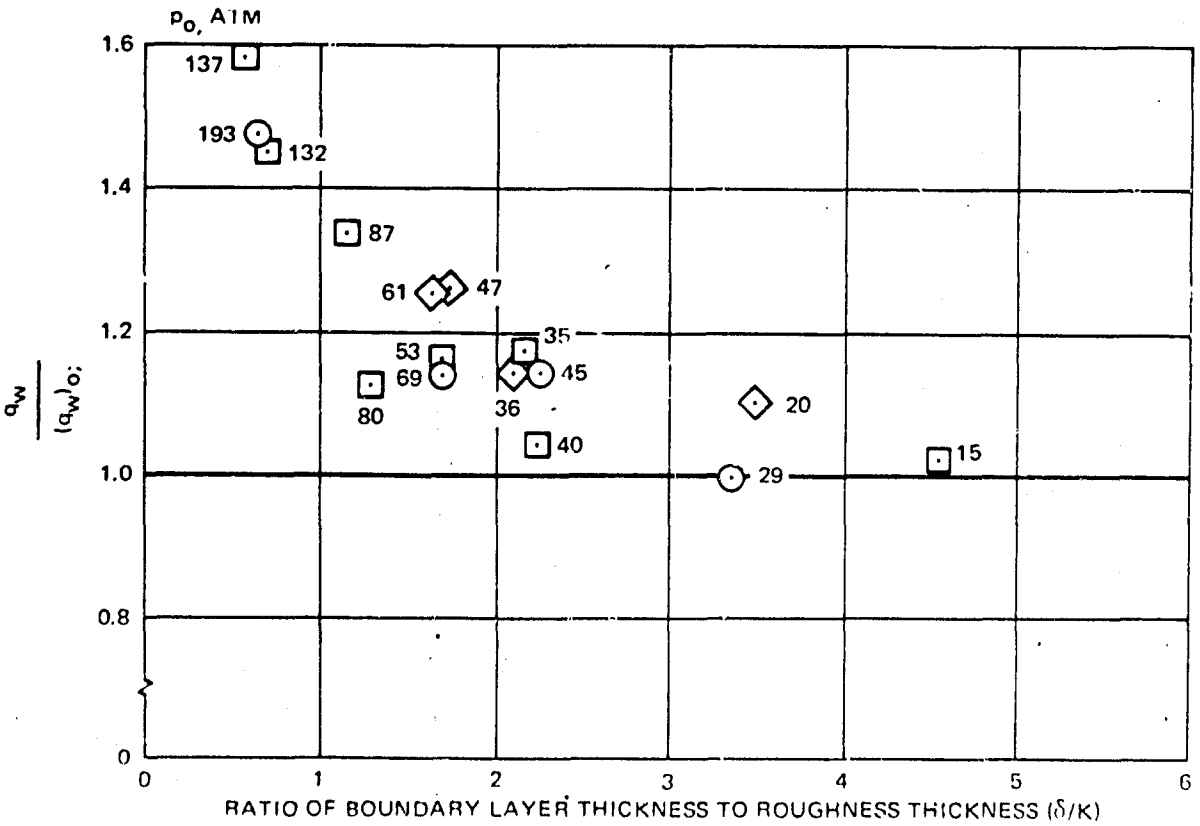

Figure 8. Heat Transfer as a Function of Boundary Layer Thickness (95)

Summation of the data presented in references 80 through 95 does not provide any insight into the mechanisms which produce the roughness elements. Knowledge of the material processes, grain size distribution, impurity content, etc., coupled with a reliable and detailed theoretical ablation model, could provide this insight. In addition, proper characterization of the material constituents, coupled with a systematic definition of the degree of roughness required to produce turbulence, could result in the tailoring of materials so that laminar flow would predominate throughout the trajectory.

3.3 Graphite Microstructure Characterization

Considering the complex material-environmental interaction postulated in section 3.2, a new and dynamic approach to analyzing the ablation performance of heterogeneous materials is in progress. This approach embodies characterizing the material microstructural quantities and employing the results to evaluate individual erosion mechanisms and finally their combined effect on high pressure ablation phenomena.

This section summarizes several of the salient features of this approach and illustrates the methodology employed by presentation of typical characterization results. The illustrations are centered around the various material variables which may be of consequence in the total ablation behavior of graphite. The analysis techniques necessary to ensure a self-consistent set of characterization parameters are addressed and examples cited which typify their application to interpretation of the erosion behavior of graphite. The data presented are not intended to represent a complete analysis which is still in the development stage, but to indicate the many facets of this new and unique approach to understanding and analyzing the ablation behavior of complex materials.

3.3.1 Micro- Macroporosity

Porosity of graphitic materials may play an important role in determining thermochemical and thermomechanical erosion. Considerable effort to develop reliable methods of characterizing the porosity of aerospace-grade graphites is required. This effort is complicated because of the wide size range of pores that may occur in a single material. In particular, two types of porosity are apparent. The first type arises from stacking disorder in the flour during the graphitization process. These stacking disorders produce voids which may be only partially filled by binder material. The resulting macropores are of the same order of size as the filler particles. Additionally, microporosity interlaced throughout the binder material is introduced during graphitization because of the formation of shrinkage cracks and local separation (debonding) of the binder from filler particles. This porosity is characterized by pores in the submicron size range.

An approximate measure of the distribution of pore volume as a function of pore radius can be obtained from porosimetry measurements. In these measurements the graphitic sample is immersed in a mercury bath and hydrostatic pressure varied. An effective radius for the penetrating mercury can be determined and the change in apparent volume of the mercury bath measured. The radius determined is only a qualitative measure of pore radius since photomicrographs show that pores are generally of a relatively large volume accessible through a smaller opening. A typical porosimetry measurement of ATJ graphite is shown in Figure 9.

For coarse grain graphitic materials the accessible volume distributions are characterized by two peaks. The first peak occurs at very small pore radius (less than 0.5 micron) and is indicative of the fine micropores connecting larger macropores. The macropore distribution generally peaks at from 2 to 6 microns mean pore radius. The macropore peak can be virtually eliminated by either impregnation of the material or by using finer filler particles in the mix.

3.3.2 Filler Particles

The flour or filler particles used in the manufacture of aerospace-grade graphite are important in the mechanical erosion model for graphite. It has been postulated that mechanical erosion of graphite occurs because of direct mechanical removal of filler particles from the oxidized and sublimed surface. Analyses relating this process to aerothermal environment have generally assumed that the filler particles can be characterized by a single mean size (78, 96); however, it is more likely that preferential removal of either the large or small particles in response to the applied pressure and pressure gradient is a strong function of particle size and perhaps shape. Hence, the distribution of particle sizes (Figure 10) may be a critically important factor governing the mechanical erosion of graphite in high pressure environments.

Filler particle size distribution, $n(d_p)$ denotes the number density of probability of occurrence of a specific size filler particle. A typical curve for a fine-grain graphite is presented in Figure 11. For this particular graphite the distribution is nearly normal. However, large departures from Gaussian distributions may be expected for coarser-grain filler particles. The mean particle diameter, d_{p_o}, and variance, σ_p^2, can be obtained from these data from the following equations:

$$d_{p_o} = \int n(d_p)\, d_p d\, d_p \tag{24}$$

$$\sigma_p^2 = \int n(d_p)\, (d_p - d_{p_o})^2\, d\, dp \tag{25}$$

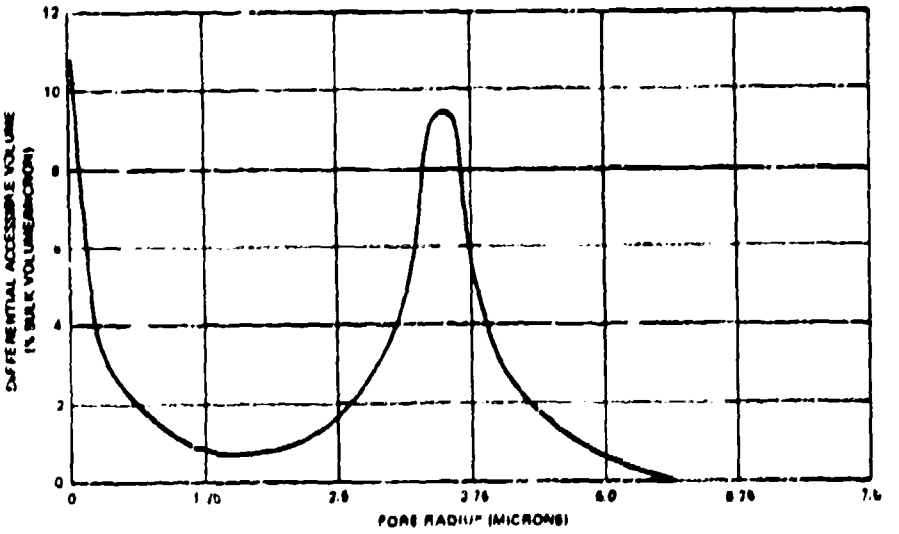

Figure 9. Porosimetry Measurement of ATJ Graphite

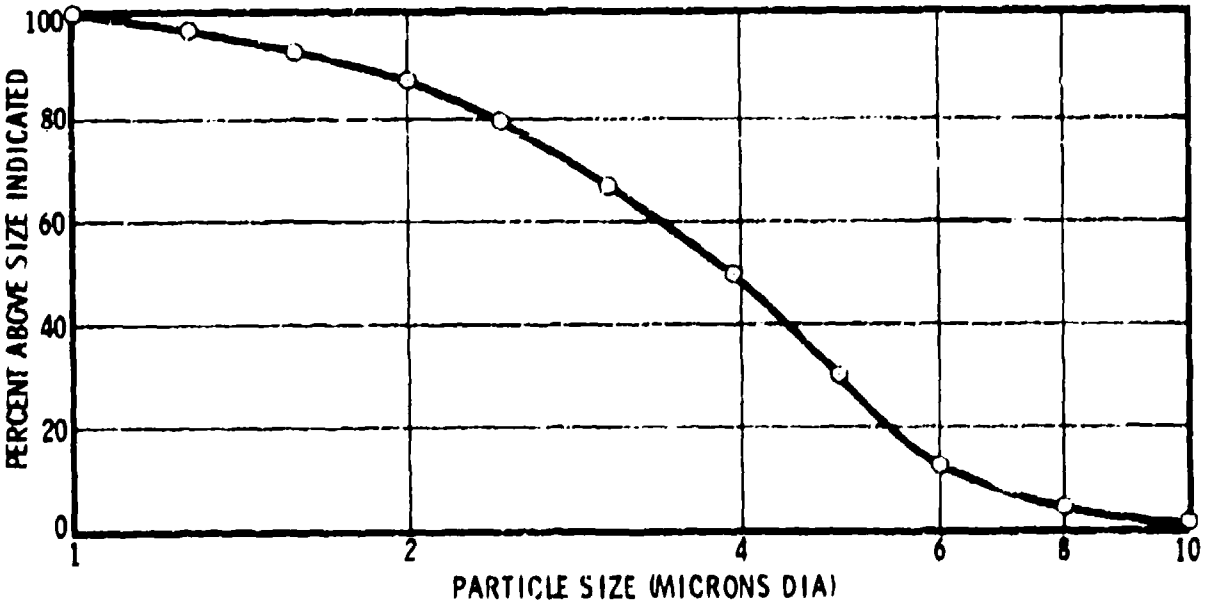

Figure 10. Typical Particle Size Distribution

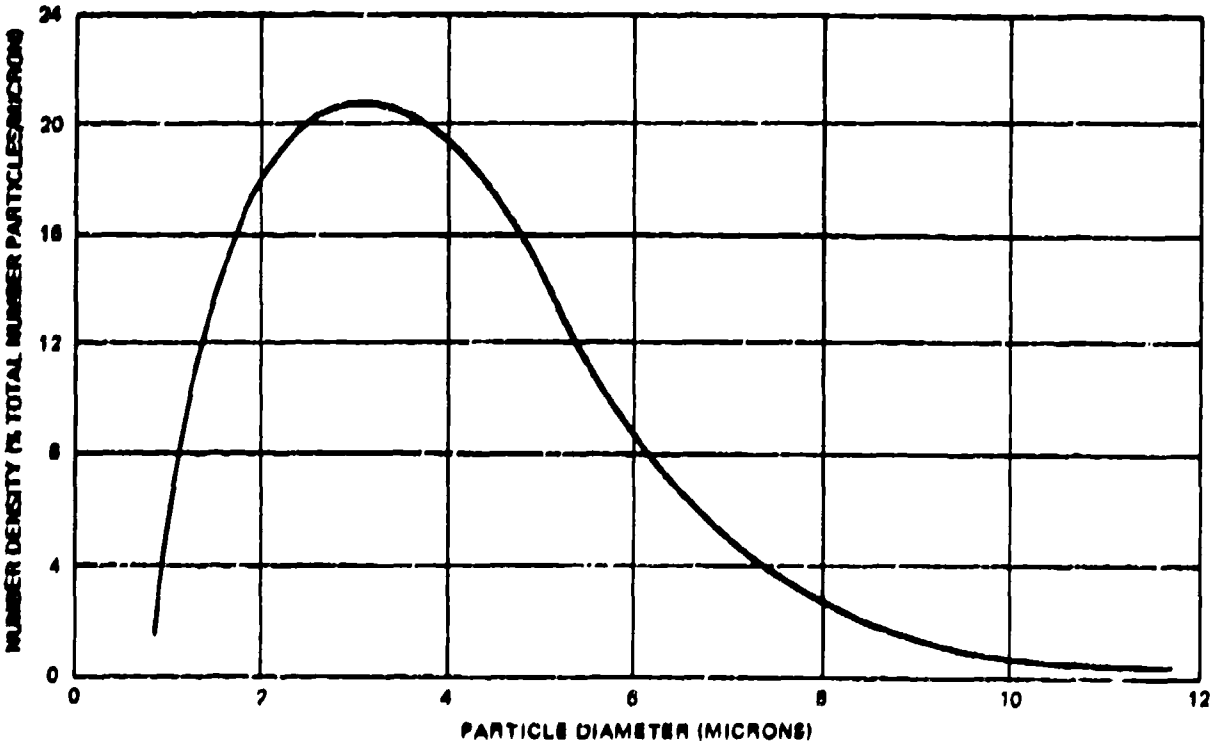

Figure 11. Number Density of Filler Particles

The mean projected area, A_{p_o}, and volume, V_{p_o}, of a filler particle can also be obtained from the second and third moments of the distribution function; that is,

$$A_{p_o} = \frac{\pi}{4} \int n(d_p)\, d_p^2\, d\, dp \tag{26}$$

$$V_{p_o} = \frac{\pi}{6} \int n(d_p)\, d_p^3\, d\, dp \tag{27}$$

For Gaussian distributions A_{p_o} and V_{p_o} are simply related to d_{p_o} and σ_p^2 by

$$A_{p_o} = \frac{\pi}{4} d_{p_o}^2 \left(1 + \frac{\sigma_p^2}{d_{p_o}^2}\right) \tag{28}$$

and

$$V_{p_o} = \frac{\pi}{6} d_{p_o}^3 \left(1 + \frac{3\sigma_p^2}{d_{p_o}^2}\right) \tag{29}$$

Additional characterization of the filler particles by a shape factor, Λ, may be required in erosion analyses. The shape factor can be defined by

$$\Lambda = \left(\frac{2\pi}{3\sqrt{3}}\right)^{1/6} \frac{N^{1/6}}{D_F^{1/3}\, a^{1/2}} \tag{30}$$

where

N = number of particles per gram

ρ_p = filler particle density

a = particle projected area per gram

These properties must be measured prior to the binder-filler mixing process. Attempts have been made to use the shape factor as defined above in a relation of the form

$$A + s\epsilon = t \tag{31}$$

where s and t are constants to determine the filler particle packing density that could be achieved in a dry state (that is, unmixed with binder). It appears clear that no such simple relation exists to determine the porosity of the graphitic materials considered for aerospace application. In particular, additional parameters entering into an expression for ϵ would include the binder mass ratio, the variance of the filler particle size distribution, and the graphitization temperature. Other than through influencing the porosity of the graphitic material, it is clear at this time that the shape factor is an important influence on erosion mechanisms.

3.3.3 Binder Properties

The primary binder properties of interest for aerothermal erosion predictions are binder bridge thickness and density. Neither of these properties can be measured directly, hence analyses have been developed to predict these properties from available characterization data. Some ambiguity usually exists in the definition of these quantities.

The binder bridge thickness is an important parameter in determining erosion rate due to sublimation and/or oxidation of binder material immediately below the surface. This can be defined as the mean thickness of binder material surrounding filler particles, macropores, and micropores. In keeping with the model of large macropores reached by small openings (micropores) both the filler particles and macropores are modeled as spheres of mean volume V_{p_o} and V_{v_o}, respectively, obtained from the respective distribution functions. The micropores are modeled as cylindrical tunnels of mean radius r_{micro_o}. The inaccessible void volume is included in the accessible macropore volume. For this model the mean bridge thickness, t_{b_o}, is given by

$$t_{b_o} = \frac{K_B}{\frac{\rho_B}{\rho}\left[\frac{2\epsilon_{micro}}{r_{micro_o}} + \frac{3(\epsilon - \epsilon_{micro})}{r_{macro_o}}\right] + 3\frac{\rho_B}{\rho_F}\frac{(1 - K_B)}{\left(\frac{3V_{p_o}}{4\pi}\right)^{1/3}}} \tag{32}$$

where

$$\rho_B = \frac{K_B\rho}{1 - \epsilon - (1 - K_B)\frac{\rho}{\rho_F}} \tag{33}$$

and ρ is the apparent density of the graphitic material, ρ_B, is the binder material density, and ϵ_{micro} is the fraction of bulk volume consisting of micropores.

The variation in mean binder bridge thickness is shown in Figure 12 for several values of the binder mass fraction, K_B, typical of various graphites. Significantly, the mean binder bridge thickness is quite thin; even a small degradation in this thickness by oxidation/sublimation may free the otherwise constrained particles resulting in their being easily dislodged from the material surface by aerodynamic forces.

3.3.4 Surface Region Macrostress

The influence of stresses on the thermomechanical erosion can be considered from both the macromechanical and micromechanical point of view. The results of stress analyses can be used to establish the macro- or micro-failure of the material and relate it to the chemical and mechanical erosion.

In addition to the porosity which is presented in the material initially, additional surface and subsurface porosity may occur. At or near the surface the internal microstructure changes drastically with time, temperature, and environment. Correspondingly any changes in the material properties at or near the surface also affect the macrostresses; not only the surface stresses but also the stresses within the body itself.

The magnitude of porosity can be estimated by the mass and heat balance relation. To a count for porosity, the material properties used for each element in a finite element analysis can be properly modified. Weil-Hashin (97) suggested the following modification:

$$\frac{E}{E_o} = \frac{1 - p}{1 + k_1 p} \tag{34}$$

$$\frac{G}{G_o} = \frac{1 - p}{1 + k_2 p} \tag{35}$$

where

$$k_1 = \frac{(1 + \nu_o)(13 - 15\nu_o)}{2(7 - 5\nu_o)} \tag{36}$$

$$k_2 = \frac{2(4 - 5\nu_o)}{(7 - 5\nu_o)} \tag{37}$$

and E_o, G_o, ν_o are the properties for dense material, E and G are the properties of the porous material and p is the porosity. For $\nu_o \sim 0.2$, $k_1 = k_2 = 1$ becomes a good approximation.

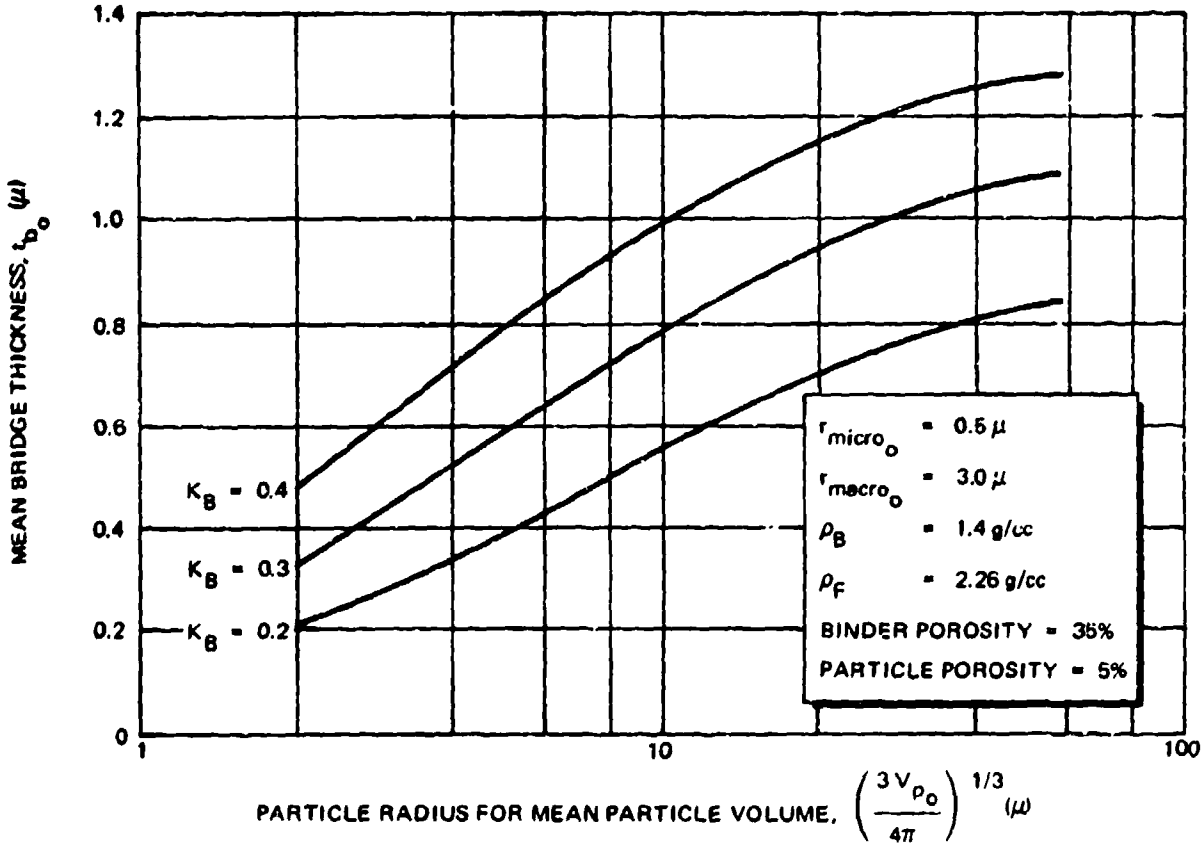

Figure 12. Variation of Binder Bridge Thickness

In addition to affecting the mechanical properties, porosity also influences the sgrength properties. As the porosity increases, the strength decreases. Some experimental results on the strength reduction due to weight loss (caused by increased porosity) of an ANL graphite are shown in Figure 13 (98). This strength reduction is predictable theoretically by the following equation (99):

$$\sigma_p = \left[1 - \frac{\pi}{4} \frac{6\, k_v^{\,2/3}}{\pi(1 - \bar{k})} \right] \sigma$$

where k_v is the volume fraction of pores, $\bar{k}$ is the volume fraction of inclusions, $(1 - \bar{k} - k_v)$ is the volume fraction of binder, σ is the strength of solid material ($k_v = 0$), and σ_p is the strength of porous material. Some typical theoretical results on the effect of k_v and $\bar{k}$ on σ_p are shown in Figure 14.

Although it is impossible to correlate results given in Figures 13 and 14 due to the fact that reference 98 did not give the inclusion content, it is quite obvious that the theory and experiment show

the same trends—a marked reduction in strength due to porosity. The results may be used to correct the physical properties entering in the macrostress analysis. With the above information available, it is possible to predict surface macrostresses and macro-failure as affected by the varying pore content which is a function of time and temperature.

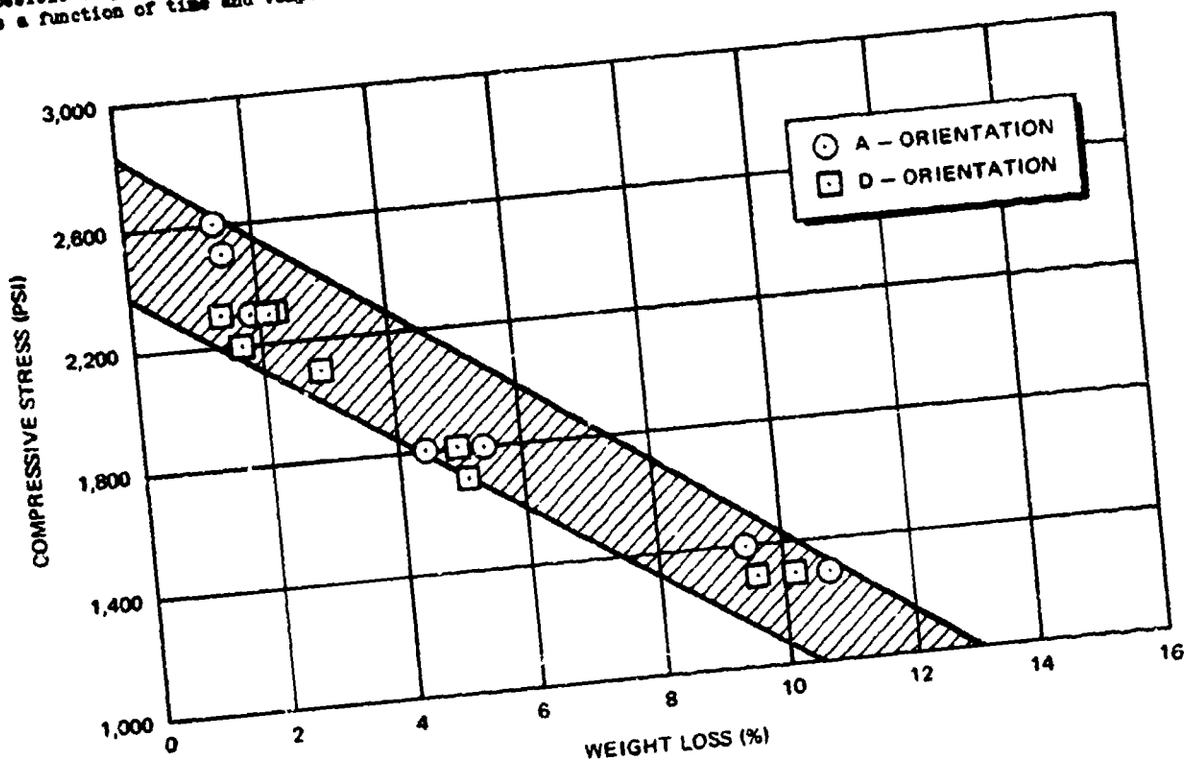

Figure 13. Change in Transverse Strength of ANL Graphite with Weight Loss Caused by Oxidation in Dry Air (98)

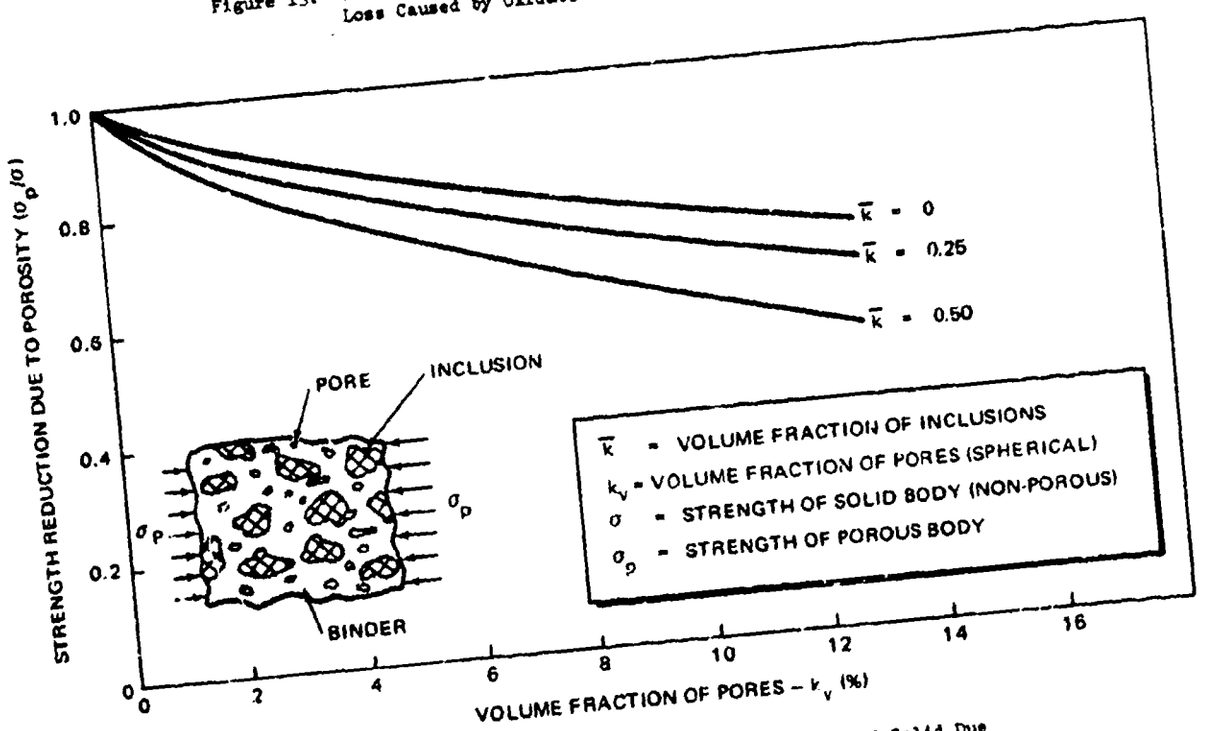

Figure 14. Strength Reduction of an Inclusion-Reinforced Solid Due to Porosity (99)

3.3.5 Synergistic Effects

The erosion behavior of graphitic materials entails an assessment of the competing chemical and mechanical mechanisms of graphite erosion and their synergistic effects. The preceding has illustrated several of the phenomena of consequence in the analytical performance description; it remains to formulate and experimentally verify the complete analytical model. At this stage, it is clear that a more thorough approach is necessary in analytical modeling of heterogeneous materials. The benefit is twofold; a rigorous ablation analysis which includes the material microstructural characteristics results and a realistic insight to the material characteristics which contribute to the observed ablation data is obtained enabling material formulations to be made, aimed at reducing or alleviating the enhanced erosion.

3.4 Graphite Thermochemical Erosion

Thermochemical erosion of graphitic materials, both in the laboratory and in ground test facilities, has been the subject of some considerable study for the past decade. At present, an incomplete understanding exists of the detailed effects of material structure on oxidation and sublimation. It is known, however, that the surface reactivity of the material is important in determining oxidation rates in the kinetic-controlled regime.

Several studies showing the effect of graphite solid structure on oxidation kinetics have been accomplished. For the most part, results are incomplete because the investigators have failed to include all possible influences on their experiments in a controlled manner. For example, both the orientation and size of graphite crystallites have been neglected in performing reduction of oxidation data.

The diffusion controlled oxidation erosion of graphitic materials in hyperthermal environments is relatively well established. The oxidation kinetic regime has been formulated by several investigators with various degrees of sophistication. The work by Welsh and Chung (100), Hearne et al. (101), and Scala (52) provides results reflecting state of the art determination of the reaction rate regime description for graphitic materials. The diffusion controlled oxidation regime and transition to this regime has been described employing both equal and unequal diffusion coefficients, utilizing similar boundary layer assumptions of Lees, the approximations of Scala and, more recently, the unequal diffusion coefficient approximation by Kendall (38). It remains that significant differences existing between the several sets of solutions, when using identical thermodynamic properties, have yet to be demonstrated.

The high-temperature thermochemical erosion regime of graphite is less well understood because of the limitation in obtaining the high temperatures required and associated temperature measurement errors. Effects of importance are vapor pressure of the carbon species evolved, the possibility of departure from phase equilibrium, incomplete definition of the experiments in terms of such considerations as reaction times, etc. The question arises, however, as to the total effect of the idealizations that are made presently on the chemical erosion of graphite. Conclusively, it can be said that the material structure has a definite effect on the chemical erosion and the importance of its detailed structure remains undetermined.

3.4.1 Vapor Properties

Considerable interest and research have been focused on the identification and thermodynamic characterization of high-temperature carbon vapor species, and elucidation of the carbon vapor equation of state in the last several years. Up until then, the thermodynamic properties of all polyatomic carbon vapor species larger than C_3 have been calculated (102, 103, 104) from the free energy increments of Pitzer and Clementi (102), which were fitted to yield a triple-point pressure of 100 atm at 4000°K (105). Likewise, the equation of state calculations (103, 104, 106, 107, 108) have failed to include the heavier molecular weight species C_{17} to C_{30}, despite evidence of their existence (109, 110) and likelihood of their prominence at high pressures and temperatures. The carbon ring molecules have also been excluded.

An extensive study of the carbon vapor thermodynamics and thermochemical ablation performance of graphite in high-pressure environments was given in reference 77. The results (77) included the thermodynamic characterization of high-temperature carbon-vapor species and the elucidation of the carbon-vapor equation of state. Heats of formation and thermodynamic properties were calculated for both the linear and monocyclic polygonal ring conformations of C_n up to C_{30} over the temperature range 100°K to 5,000°K. The thermodynamic properties of the linear and cyclic molecules C_3 to C_{30} were calculated by quantum and statistical mechanical techniques. The resonance energy of each molecule was computed from the electronic wave functions by the extended Huckel method of Hoffmann (111), and the corresponding vibrational frequencies were determined by a normal coordinate analysis of the molecular structure. The theoretical procedures employed were self-consistent and did not resort to the empirical increments adopted by Pitzer and Clementi (102) and used by others (103, 104). Figure 15 depicts the logarithms of the partial pressures of the linear molecules in phase equilibrium with graphite. The plot shows linear C_3 is the most stable species and linear C_5 somewhat more stable than C_4 and C_6, in agreement with previous mass spectrometric findings (109, 112). It is also apparent that the contribution of ring molecules is negligible (77), and that larger linear molecules become very important at 4500°K, and should be included in calculations performed above 4000°K. In Figure 15, an even-odd alternation is evidenced above C_{10} at 4000°K; the effect appears to propagate to smaller values of n with increasing temperature.

Figure 16 reflects the present state of affairs in regard to total carbon vapor pressure and several calculations that have been made in the past several years. As observed, large differences in vapor pressure exist in the temperature range 3000 to 4500°K. The calculated total vapor pressure (77) is in good agreement with the experimentally determined sublimation point of Thorn and Winslow (112) and lies between the recent triple-point temperatures of Schoessow (114) and Fateeva (115). The calculated

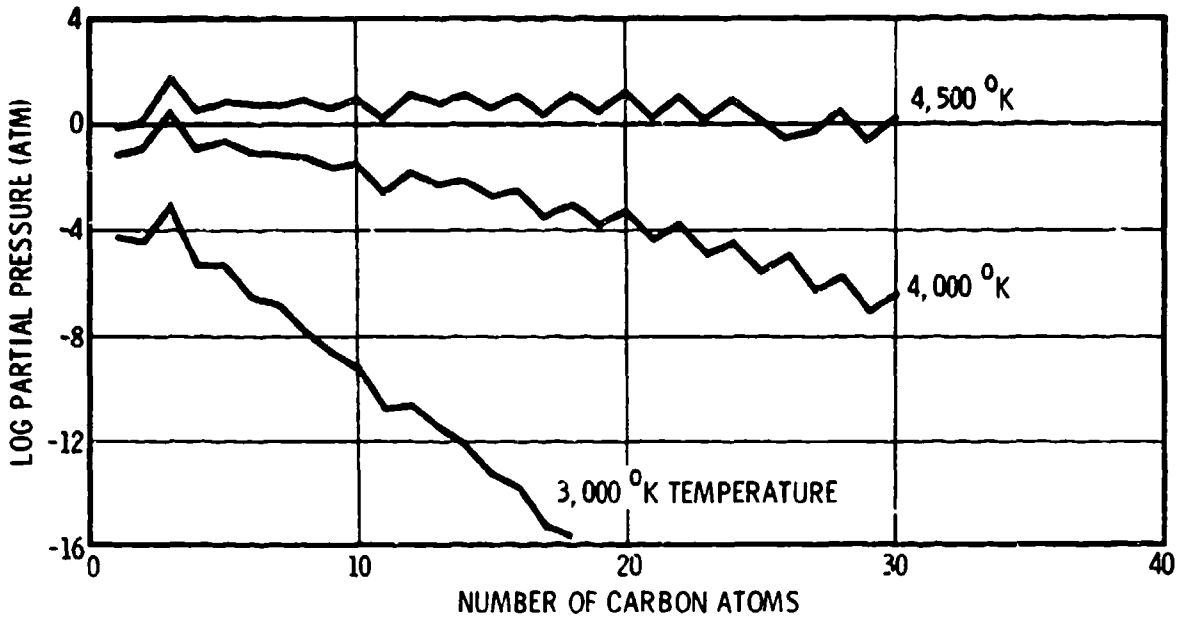

Figure 15. Partial Pressures of Linear Carbon Vapor Species

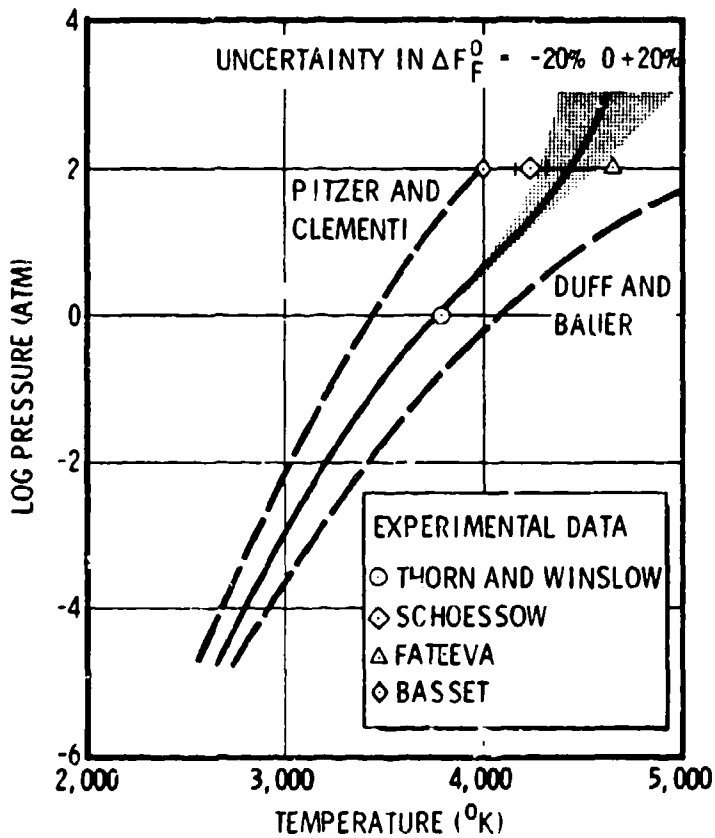

Figure 16. Graphite Equilibrium Vapor Pressure

thermodynamic properties given by Kratsch et al. (77) are entirely theoretical, and the fundamental constants employed in the claculation were utilised to establish the uncertainty in carbon vapor pressure in a self-consistent manner. This facet of self-consistency in evaluating the uncertainty in thermodynamic properties in carbon-species vapor pressure, is important and is reflected by the uncertainty in the free energies of formation for each species with $n > 3$.

3.4.2 Mass and Energy Transfer

The governing conservation equations to an ablating body with internal gas generation has been stated in section 2.2. Their application to graphite is applied in this section.

The elemental mass balance of a material consisting of i-chemical elements whose surface recedes at a rate s and undergoing loss of solid material, m_r, at the surface (Figure 1) is given by

$$\dot{m}_g \tilde{K}_{i_g} + \dot{m}_s \tilde{K}_{i_s} - \dot{m}_r \tilde{K}_{i_r} - (\rho v)_{i_w} = 0 \tag{38}$$

where $\dot{m}_g \tilde{K}_{i_g}$ and $\dot{m}_s \tilde{K}_{i_s}$ are the mass fluxes of the element i into a control volume fixed at the receding surface owing to an internal gas source and solid material transfer, respectively. Mass leaves the control volume normal to the wall by a net flux of gas, $(\rho v)_{i_w}$, and by loss of solid, $m_r \tilde{K}_{i_r}$. The mass flux of the ith element normal to the wall accrues by a summation of individual flux components consisting of the internal gas source, surface chemical reactions with the external reactive gas (boundary layer and internal gas species) and by direct sublimation. For graphite in an air boundary layer the following conservation statements are made at the wall (77):

$$\tilde{K}_{N_w} + \tilde{K}_{O_w} + \tilde{K}_{C_w} = 1 \tag{39}$$

$$(\rho v)_{C_w} = \rho v_w = \rho v_w \tilde{K}_{C_w} - \left(\frac{\rho D \partial \tilde{K}_C}{\partial y}\right)_w \tag{40}$$

$$(\rho v)_{O_w} = 0 = \rho v_w \tilde{K}_{O_w} - \left(\frac{\rho D \partial \tilde{K}_O}{\partial y}\right)_w \tag{41}$$

$$(\rho v)_{N_w} = 0 = \rho v_w \tilde{K}_{N_w} - \left(\frac{\rho D \partial \tilde{K}_N}{\partial y}\right)_w \tag{42}$$

The gradient of the individual chemical elements at the wall is given by, e.g., carbon

$$\left(\frac{\partial \tilde{K}_C}{\partial y}\right)_w = \left(\frac{\tilde{K}_{C_e} - \tilde{K}_{C_w}}{H_{S_e} - H_w}\right) \left(\frac{\partial H}{\partial y}\right)_w \tag{43}$$

and for unity Lewis-Semenov number the convective heat transfer to the wall by conduction and diffusion is, upon introduction of Stanton number

$$\dot{q}_{conv} = \left(\frac{k}{C_p} \frac{\partial H}{\partial y}\right)_w = \rho_e u_e C_H \left(H_{S_e} - H_w\right) \tag{44}$$

Thus, Eq. 38 can be solved by introducing Eq.s 40, 43, and 44 and, after rearrangement, the elemental mass fraction of carbon at the wall is given by

$$\tilde{K}_{C_w} = \frac{\tilde{K}_{C_e} + \frac{\dot{m}_g \tilde{K}_{C_g}}{\rho_e u_e C_H} + \frac{\dot{m}_s \tilde{K}_{C_s}}{\rho_e u_e C_H} - \frac{\dot{m}_r \tilde{K}_{C_r}}{\rho_e u_e C_H}}{1 + \frac{(\rho v)_w}{\rho_e u_e C_H}} \tag{45}$$

where for graphite in an air boundary layer

(46)

$$\rho v_w = \dot{m}_g + \dot{m}_s - \dot{m}_r$$

$$\bar{K}_{C_e} = 0 \qquad \bar{K}_{C_g} = 1$$

$$\bar{K}_{N_e} = 0.768 \qquad \bar{K}_{C_s} = 1 \tag{46}$$

$$\bar{K}_{O_e} = 0.232 \qquad \bar{K}_{C_r} = 1$$

The fraction of solid entering the control volume which is lost at the surface as particulate solid is defined from Eq. 46

$$\rho v_w = \dot{m}_g + \left(1-f_s\right)\dot{m}_s$$

$$\dot{m}_r = f_s\,\dot{m}_s \tag{47}$$

Inspection of Eq. 45 shows that the mass fraction of the element carbon at the wall is determined solely by the mass flux of elemental carbon injected at the surface as vapor, reflected by the difference in fluxes entering and leaving the control volume. Equations similar to Eq. 45 for the element oxygen and nitrogen provide the necessary relations satisfying Eq. 39. A stoichiometric statement then directly relates the elemental mass fractions to the chemical composition of the combustion-sublimation species at the ablating surface

$$\bar{K}_i = \sum_j \frac{\nu_i\, M_i}{M_j}\, K_j \tag{48}$$

Numerical solutions to the governing equations were given in (77) invoking the chemical equilibrium constraint. The chemical reaction system included sublimation species for the ring and chain molecules, and in addition air species, and carbon-air reaction products listed below

O	NO	CO_2
O_2	N_2O	CN
N	NO_2	C_2N_2
N_2	CO	C_4N_2

Graphite sublimation rates over a large pressure range are shown in Figure 17 normalized to the familar diffusion-controlled oxidation rate ($m_D = 0.174\ \rho_e u_e\ C_H$). In the first several decades of pressure the threshold sublimation temperature increases with increasing pressure reflecting the carbon-vapor-pressure diagram shown in Figure 16. The 10^1 to 10^3 atm pressure range is of special interest; the threshold sublimation temperature is compressed due to sublimation of large quantities of polyatomic carbon-vapor species. Thus, the high-pressure sublimation regime of graphite occurs over a fairly narrow surface temperature range (circa 7000-8000°R) in contrast to Scala's (52) results (7000-10000°R) which omit carbon molecules larger than C_3. Upon definition of a surface-energy balance and the indepth heat conduction, sublimation rates are directly coupled to surface temperature and pressure and the local aerodynamic heating.

Energy transfer to a surface undergoining material consumption via thermochemical erosion and thermomechanical loss of solid is given by an energy balance, Figure 1. The heat conducted by the solid away from the surface reflects the energy fluxes leaving and entering the control volume expressed in the following:

$$\dot{q}_{conv} + \dot{q}_{\substack{rad\\in}} - \dot{q}_{\substack{rad\\out}} - (\rho v)_w\, H_w - \dot{m}_r\, H_s = \dot{q}_{cond} - \dot{m}_g\, H_g - \dot{m}_s\, H_s \tag{49}$$

where

$$H_w = \sum_j K_j\, H_j$$

$$H_j = \int C_p dt + \Delta H_F^\circ \tag{50}$$

The summation in Eq. 50 is made over all species in the gas at the wall with concentrations defined by the mass-transfer rates and application of the equilibrium constant. For the case of Le = 1 the net heat transfer to the surface may be expressed as (at this time $\dot{m}_g$ is set equal to zero)

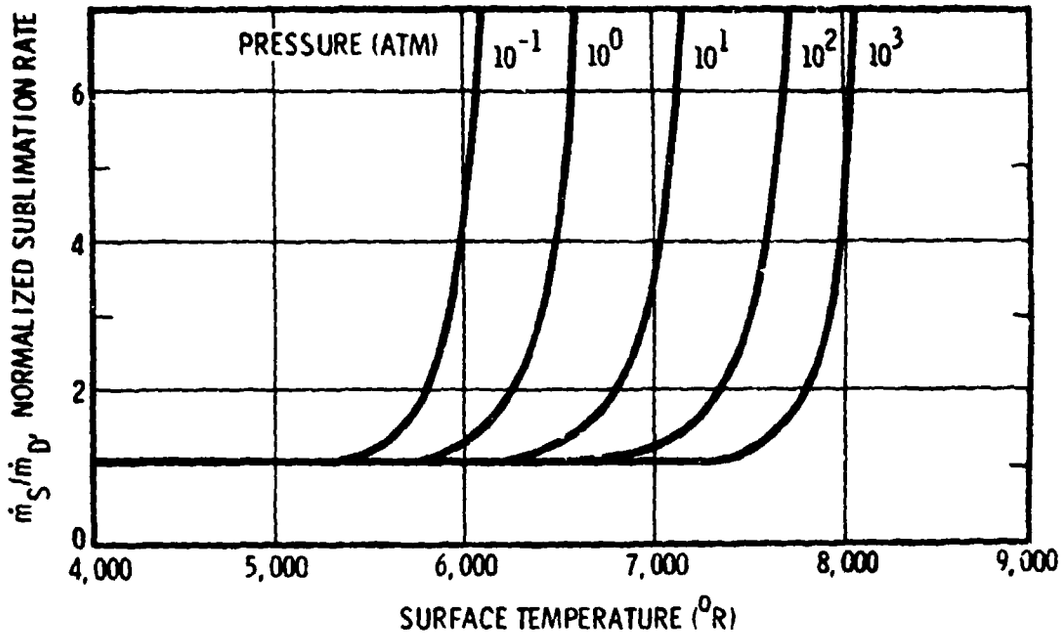

Figure 17. Graphite Sublimation Rate

$$\dot{q}_{cond} = \rho_e u_e C_H \left[H_{S_e} + (1-f_s) \; B'_s H_s - (1+B'_w) \; H_w \right] + \dot{q}_{\substack{rad \\ in}} - \varepsilon\sigma T_w^4 \tag{51}$$

when the usual definition of the mass transfer parameter is made

$$B' = \frac{\dot{m}}{\rho_e u_e C_H} \tag{52}$$

Eq. 51, when coupled to a standard finite difference solution to the conduction equation enables a complete description of the surface erosion of graphite including solid loss. It is observed that the effect of solid removal on the surface energy balance is to reduce the net energy transfer. For example, at a surface temperature of 7500°R the $B'_s H_s$ term is about 1700 Btu/lb at 100 atm pressure; Eq. 51 is reduced only by 850 Btu/lb for $f_s = 0.5$. In comparison, the enthalpy of the combustion-sublimation products at the ablating surface is about 400 Btu/lb as shown in Figure 18. The enthalpy of the gaseous products (given by Eq. 50) evidences the exothermic CO chemical reaction product below 5000°R surface temperature. The increase in enthalpy above 5000°R is coincident with sublimation; highly endothermic carbon vapor species evolve at the surface.

Detailed results of the high-pressure sublimation regime are shown in Figure 19. The chemical composition at the ablating graphite surface is given at 100 atm pressure. In addition to the air-carbon reaction products, a complex set of sublimation species is evidenced. The triatomic carbon-molecule is most abundent; however, a large number of polyatomic molecules of rather low concentration are seen. Other than C_3 the prevalence of any single carbon vapor species is not evident. Although vapor species having ring structures were included in the numerical computations, the concentrations shown are due only to linear structured molecules. Conclusively, the ring molecules can be safely neglected in performance analyses for graphitic materials. Omission of the linear carbon species at high pressures examined here may be quite critical as affects mass transfer (77).

It is interesting to examine how the ablated mass of carbon is partitioned among the chemical composition shown in Figure 19. In Figure 20 the elemental mass fraction of carbon is shown extending from the diffusion-controlled oxidaton regime well into the sublimation regime. As indicated, the constant mass fraction of 0.15 reflects the carbon mass in CO. At about 6500°R nitrogen reacts forming the cyano radical

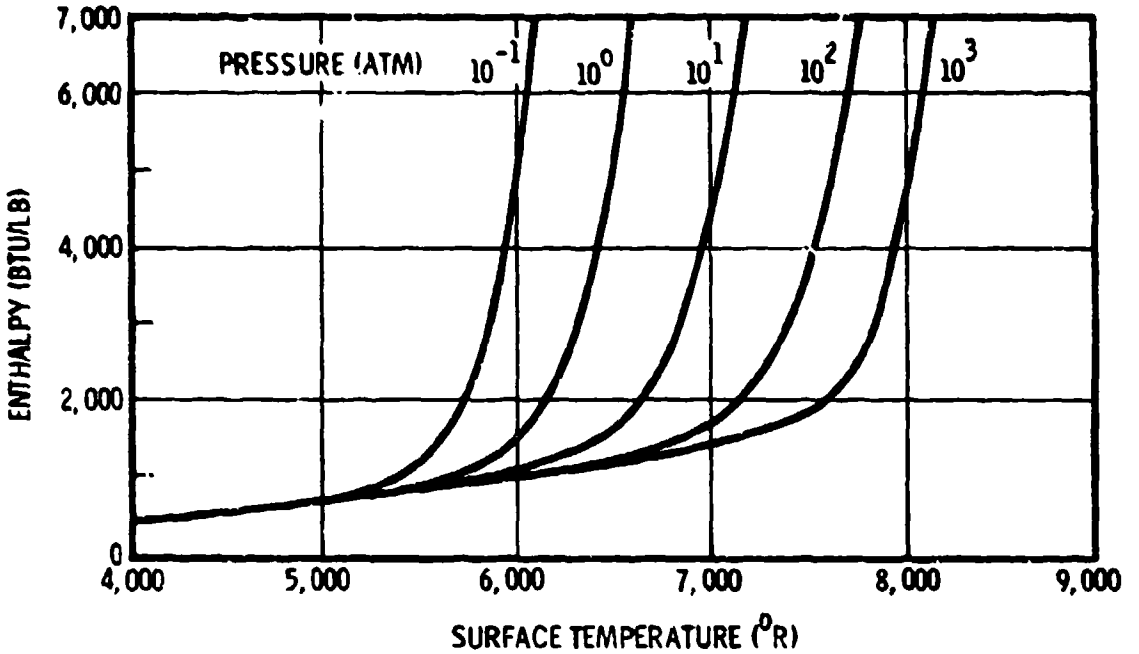

Figure 18. Enthalpy of Combustion-Sublimation Products at Ablating Graphite Surface

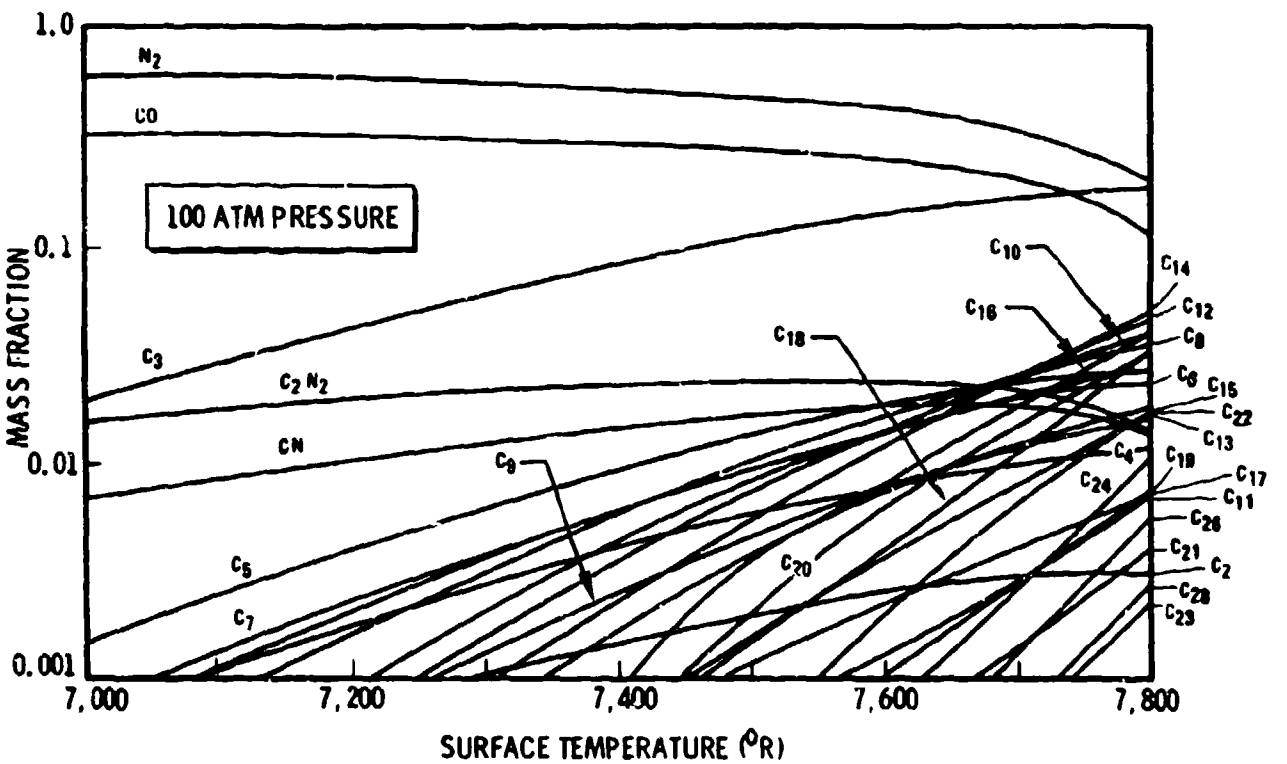

Figure 19. Chemical Composition at Graphite Surface

and cyanogen; only a small mass of carbon is ablated because of these reaction products. At about the same temperature (6500°R) contributions due to C_1 to C_3 occur, increasing the mass fraction of ablated carbon. With increased temperature larger carbon vapor species sublime from the surface appearing first as species having from 4 to 10 carbon atoms and then in species having from 11 to 20 carbon atoms. For the 100-atm pressure condition shown, little contribution from vapor species with greater than 20 carbon atoms occurs. More clearly than indicated in Figure 19, it is apparent that the additive small concentrations of the polyatomic carbon vapor species is quite appreciable.

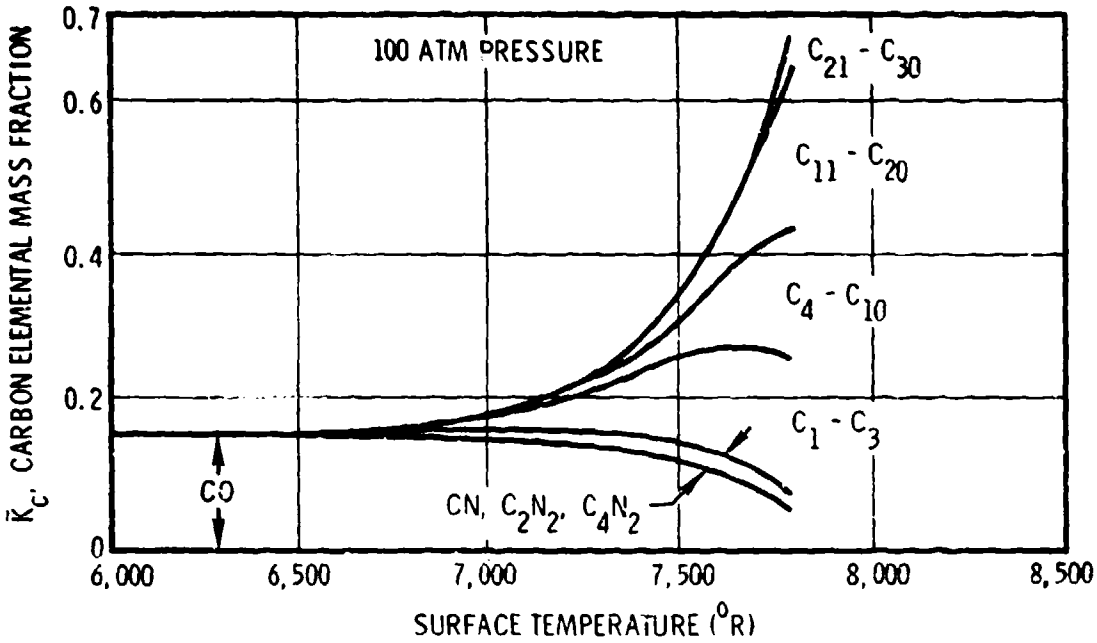

Figure 20. Partition of Elemental Mass Fraction of Carbon with Surface Temperature

3.4.3 Sensitivity Analysis

The uncertainty limits established for the carbon-vapor species as affects mass transfer and energy transfer can be assessed employing the conservation equations previously described. Figure 21 the normalized sublimation rate for several pressures included ±20 percent uncertainty in free energy of formation for the carbon-vapor species. The uncertainty band reflected in Figure 21 is consistent with the vapor pressure diagram shown in Figure 16; the higher pressure evidences a greater uncertainty band due to the greater concentration of sublimation species. For comparative purposes, results calculated by Scala (52) are shown for a normalized sublimation rate of 4.0. Also shown are results by Dolton et al. (104) at 1 atm pressure. He includes vapor species up to C_{16}, employing empirically determined free energies forced to fit a presumed 4000°K triple-point temperature. It is seen that, at 100 atm pressure and for constant surface temperature, sublimation rate can be as much as 3 times larger than the nominal value. The effect of uncertainty in thermodynamic properties, diminishes with decreased pressure, owing to the smaller vapor-pressure contribution of the high molecular weight vapor products. Corresponding results showing the effect of the combustion-sublimation products on wall enthalpy, are shown in Figure 22. The composite of these results enable an assessment of the uncertainty on surface recession rate to be made.

The calculated surface recession rate for a range of environmental conditions studied in correlation of high-pressure test data (77) is shown in Figure 23. At the highest stagnation enthalpy shown (10,000 Btu/lb) calculated surface temperature is 7500°R at 100 atm pressure. The sensitivity of surface recession, owing to the uncertainty band on properties, is small. This sensitivity decreases with both reduction in stagnation enthalpy and pressure, evidencing the effect shown in Figure 21 on sublimation rate. Even though a large uncertainty in the thermodynamic properties of the carbon vapor species was included (resulting in almost a decade uncertainty in carbon-vapor pressure) the effect on surface recession is less than 10 percent within the environmental conditions discussed. This result occurs because of the counter-balancing effect of increased endothermic heat absorption when greater quantities of carbon vapor are evolved at the surface. Thus, when using a self-consistent model for calculating the vapor species

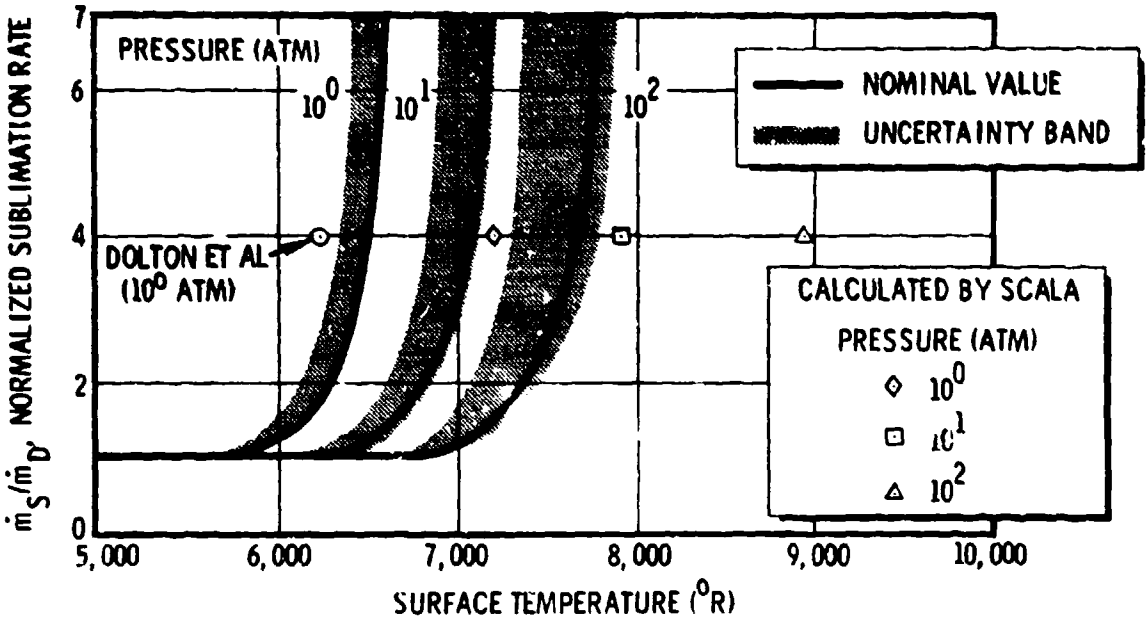

Figure 21. Graphite Sublimation Rate Sensitivity to ±20% Uncertainty in ΔF_F°

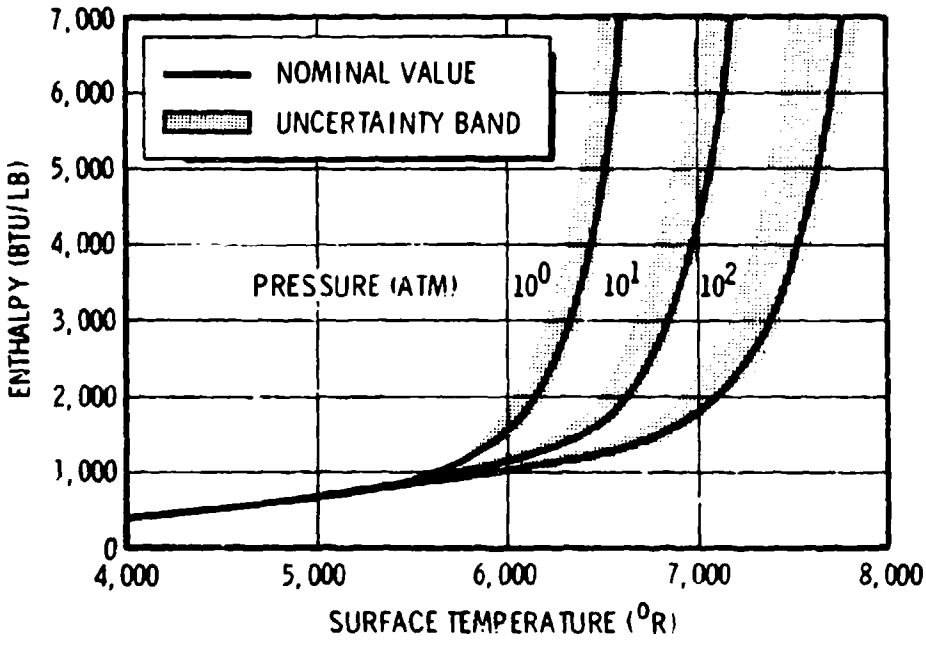

Figure 22. Sensitivity of Enthalpy of Combustion-Sublimation Products at Ablating Graphite Surface to ±20% Uncertainty in ΔF_F°

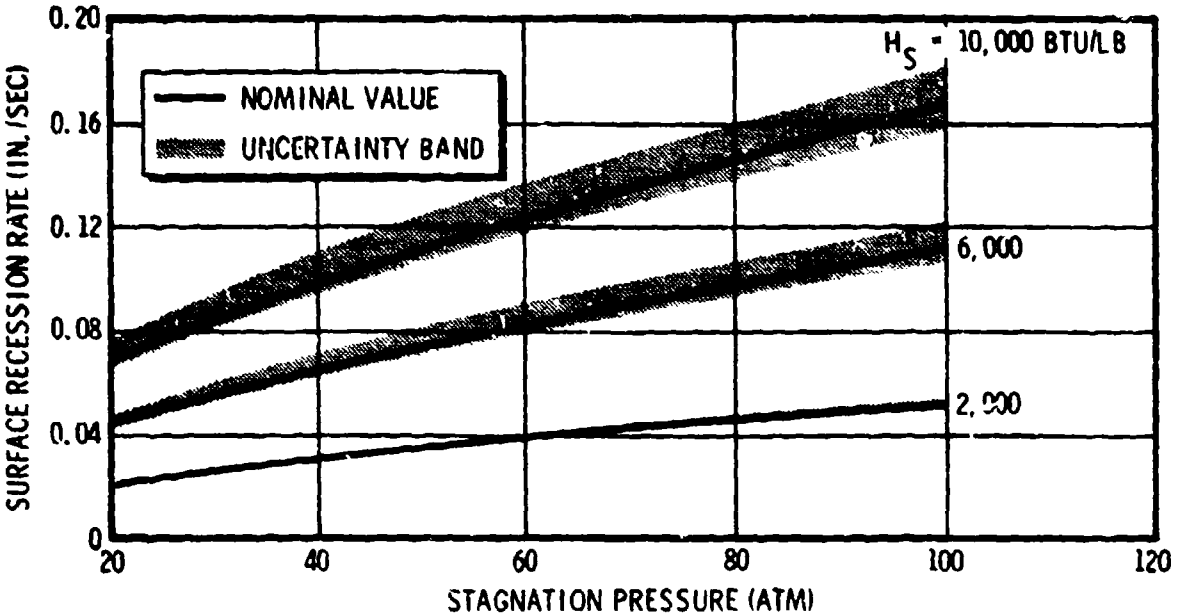

Figure 23. Thermochemical Surface Recession Rate

thermodynamic properties with associated uncertainty [illegible] ..ivity on surface recession is comparable to the accuracy for which local aerodynamic heating co[illegible]..ions can be defined.

3.5 Graphite Mechanical Erosion

This section presents the mechanical erosion aspects of graphite given in (77) and is devoted to determination of the fraction of particulate solid eroded from the receding surface in terms of environmental exposure conditions. To accomplish identification of the thermomechanical recession component from surface erosion measurements of the test data, the thermochemical recession data described in section 3.4 is used. The probable uncertainty in thermodynamic data employed on surface recession rates was evaluated in a description of sublimation rates. Loss of particulate solid at the heated surface is addressed in this section as affects mass and energy transfer. Correlation of the experimental data in terms of thermochemical erosion enables quantitative identification of the solid fraction eroded.

3.5.1 Ablation Data

Representative graphite plasma arc ablation data given in (77) is presented for completeness. A typical block of data is shown in Figure 24; experimental recession data are plotted against apparent stagnation enthalpy. Two sets of data are given as typical. Shown are data taken in the stagnation pressure range of 83.5 to 88.6 atm and data gathered between 18.6 and 23.1 atm. Each set of data was correlated (77) using a least squares curve fit of the data points. Results similar to these have been obtained for nominal stagnation pressures of 55 and 70 atm. The composite of the recession data enables construction of the experimental recession rate map shown in Figure 25. Here experimental recession rate is shown in terms of stagnation pressure and stagnation enthalpy. Figure 25 presents the total picture of the dependency of the experimental recession rate data upon the environmental conditions, stagnation enthalpy, and pressure. The data appear to be linear functions of pressure and enthalpy.

Construction of the experimental recession data map enables a comparison of the calculated thermochemical recession to the observed experimental recession data. Figure 6 presented the ratio of experimental and thermochemical mass fluxes for the test environmental spectrum shown in Figure 25.

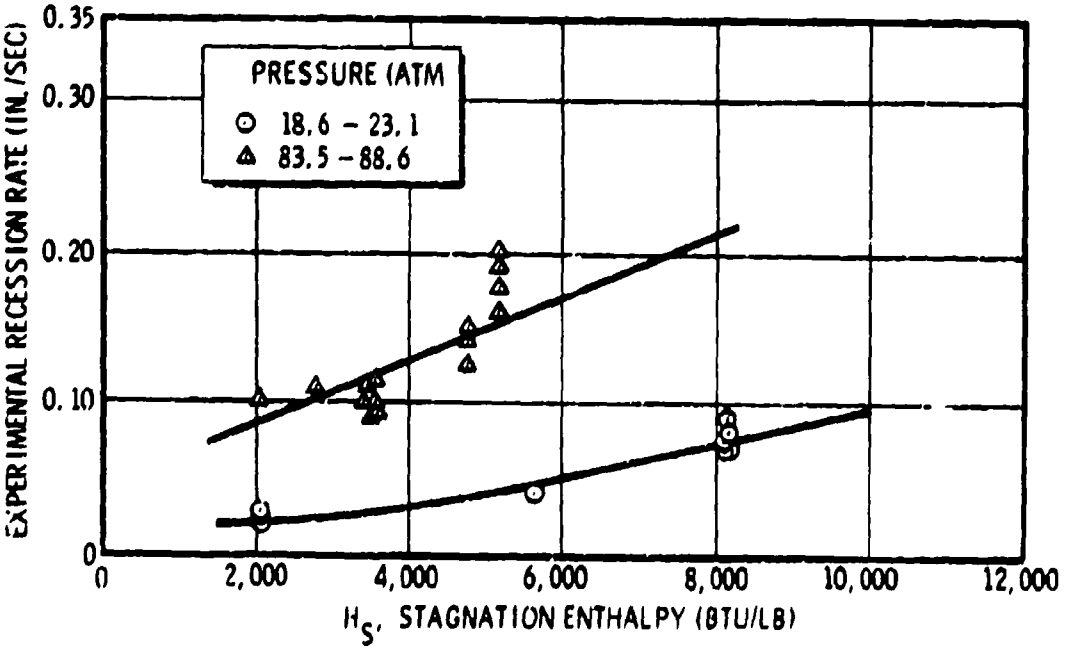

Figure 24. Experimental Recession Rate Data

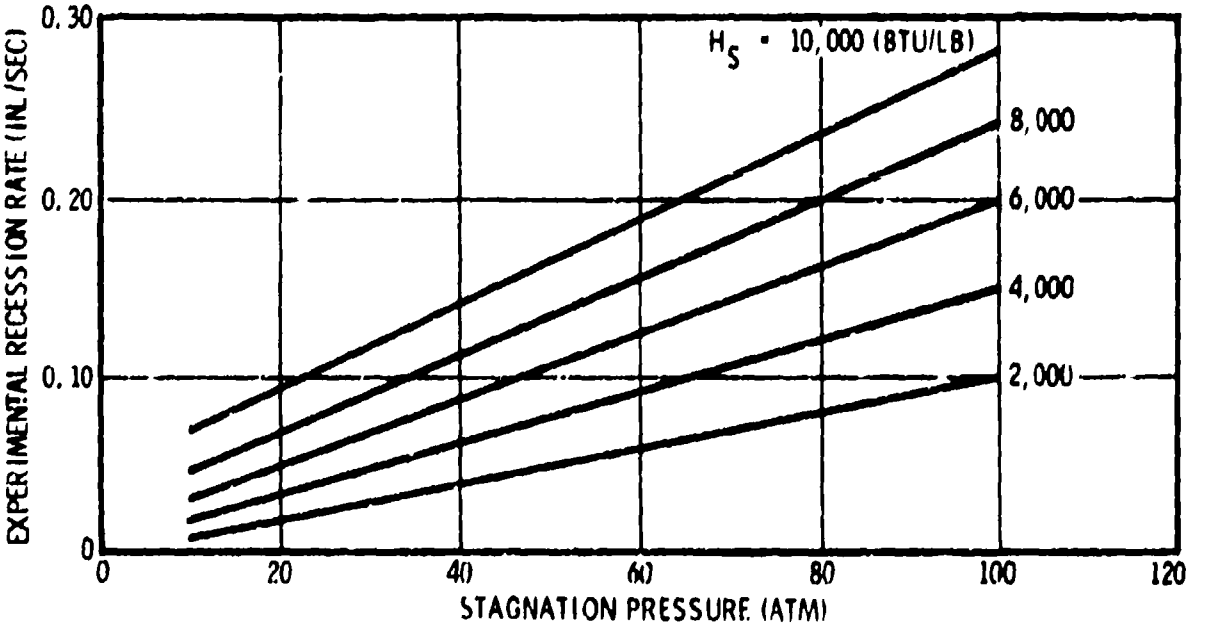

Figure 25. Experimental Recession Rate Data Map

3.5.2 Solid Fraction Eroded

Figure 26 shows the departure from thermochemical erosion in more meaningful terms. From the composite of experimental data and numerical results, including solid removal, the fraction of solid eroded has been calculated and is depicted in Figure 26. The threshold stagnation pressure at which loss of particulate solid initiates is dependent on stagnation enthalpy (reflecting convective heat rate at constant pressure). The results shown are consistent with those expected, increased stagnation enthalpy results in higher surface temperatures; hence, greater subsurface loss of binder material reducing binding of filler particles within the graphite matrix. Increasing pressure above the threshold value causes a large increase in the solid fraction eroded over a fairly narrow pressure range. The increment in solid eroded thereafte, decreases as the full pressure range is covered.

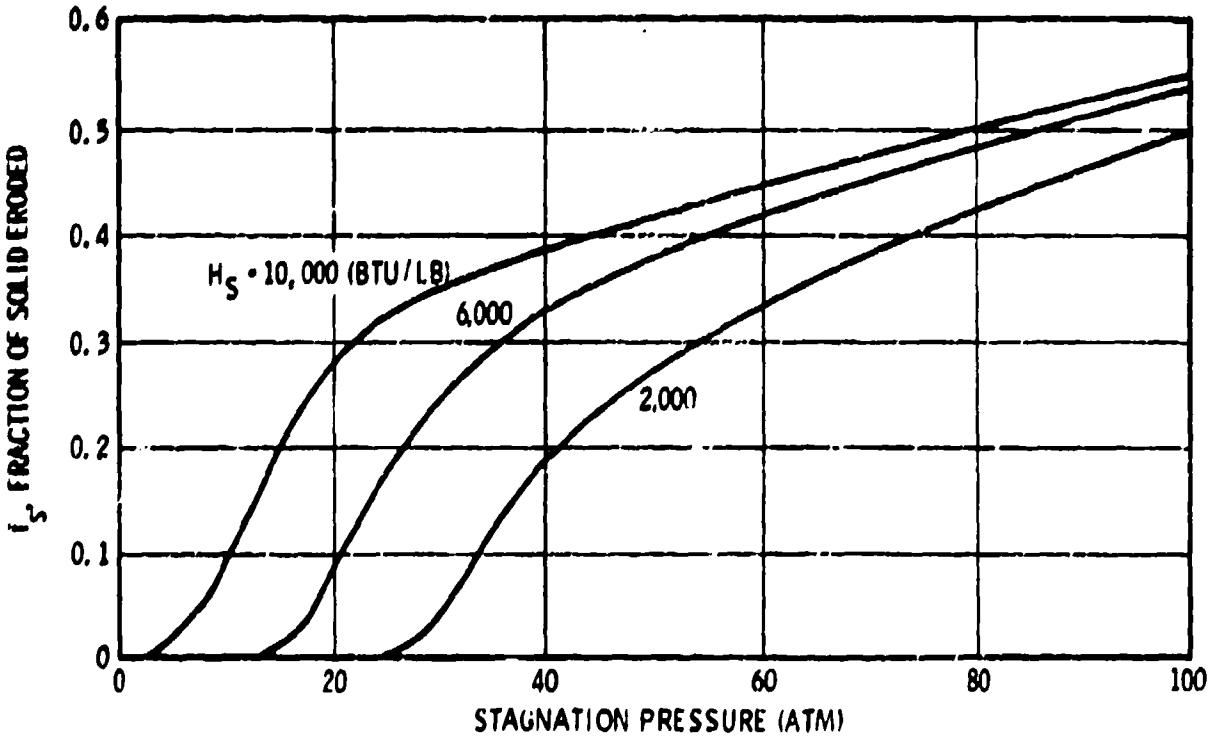

Figure 26. Fraction of Solid Eroded From Experimental Data

Complementary results are given in Figure 27 depicting the predicted surface temperature as affected by loss of solid from the heated surface. Noteworthy, is the rather small decrease in surface temperature for even large fractions of solid eroded. Surface temperature is most affected by solid loss at the low stagnation enthalpy; the high stagnation enthalpy somewhat masks the less efficient removal of material in the solid state.

To interpret the results in Figure 26 in terms of the contents of this review, reference is made to the postulated preferential erosion mechanisms previously discussed. First, it was observed that the effect of pressure on surface temperature is small at the respective values of stagnation enthalpy (within the pressure range covered). Thus, each value of stagnation enthalpy can be viewed in terms of nearly constant surface temperature for the range of solid fraction eroded evidenced in Figure 26. Consider then the role of stagnation pressure, the normal force acting on the heated surface. As the surface recedes, filler particles of various size are continuously exposed. Loss of binder below the heated surface and by direct thermochemical erosion at the surface tends to free the otherwise constrained and somewhat interlocked particles. The larger filler particles are then rather easily blown free by even moderate pressures, commencing with the higher temperature exposure conditions (i.e., stagnation enthalpy) with increased pressure acting to free the smaller particles. Also, minute amounts of binder leave the surface attached to the dislodged filler particles. As indicated in Figure 26 the effect of enthalpy (hence, surface temperature) at the higher pressures appears to diminish and pressure dominates the loss of particulate solid. Interestingly, the fraction of solid eroded appears to be approaching an asymptotic value in the range 0.6 to 0.8. Significantly, the nominal mass fraction of filler particles (about 0.75) falls within this range. Finally, the effect of aerodynamic shear and pressure gradients typical of positions removed from the stagnation point is to induce increased particle loss. Thus, one

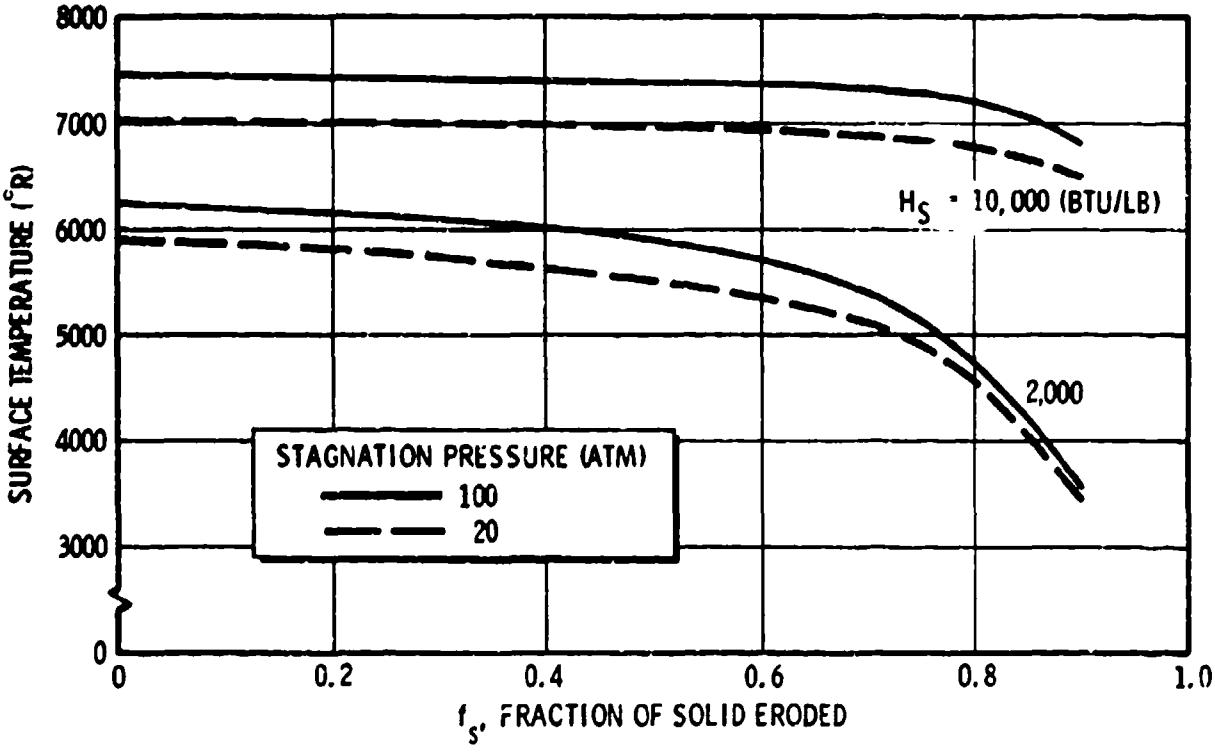

Figure 27. Influence of Solid Fraction Eroded on Surface Temperature

is faced with loss of particulate graphite over a rather broad range of aerodynamic conditions, perhaps even extending into the relatively moderate super-orbital entry environment.

3.6 Conclusions and Recommendations

A model incorporating the allotropic features of bulk graphite has been postulated and used to describe the continuous removal of particulate graphite from the heated surface. Although hypothetical in its formation, sufficient laboratory data are advanced to establish the creditability of removal of filler particles in the solid state. The key role of the different forms of carbon in graphite on surface erosion has been established. Thermodynamic properties of the linear and cyclic molecules C_3 to C_{30} were calculated by quantum and statistical mechanical techniques. The resonance energy of each molecule was computed from the respective electronic wave functions, and the corresponding vibration frequencies were determined by a normal coordinate analysis of the molecular structure. The theoretical procedures are self-consistent, resort to the empirical increments adopted by Pitzer and Clementi and used by others has been avoided. The agreement of the calculated vapor pressure with the triple-point and sublimation data is excellent. By purely analytical means, the uncertainty in the free energy of formation has been established; the effect on calculated thermochemical surface recession was found to be small. Significantly, this result has enabled identification of the solid fraction of graphite eroded in high-pressure ground tests with confidence.

To establish the solid fraction of particulate graphite eroded ablation data encompassing fine to coarse grain graphites have been correlated. The loss of material in the solid state has been determined over a range of environmental conditions (in terms of stagnation pressure and enthalpy) evidencing large fractions of solid removal. Loss of particulate solid initiates at rather low stagnation pressures; the actual threshold is dependent on heating rate as well as pressure. The mechanisms by which loss of particulate graphite occurs appears to be by preferential surface recession and subsurface loss of binder matrix. Filler particles are then easily dislodged from the surface by even moderate forces (i.e., pressure, shear). Surprisingly, the loss of solid at the heated surface does not appreciably depress surface temperatures, even for rather large fractions of solid loss.

The results presented in this review (77) open several interesting avenues for pursuit. Clearly, the role of graphite microstructure in dictating surface erosion cannot be dismissed. Closely related to the microstructure of the binder and filler phases are the thermophysical, mechanical, and chemical properties which individually, or in combination, affect ablation performance. Future analyses employing statistical distributions of particle size, void size and spacing, and accounting for the temperature-time course of the crystallite growth will be necessary before a completely analytical performance description of graphite can be achieved. Finally, new graphites overcoming the evident dissimilar characteristics of the constituent materials appear to afford a means of reducing or alleviating preferential erosion, hence, loss of solid material.

4.0 MATERIALS BEHAVIOR AND TESTING

The importance of materials characterization in the study of ablation phenomena cannot be over emphasized. Since most applications require specialized materials and since each environment interacts differently with the ablator, it may be said that each ablation theory is fathered by development of an improved ablator. It is desirable to review factors which affect the ablation performance of material, sensitivity of ablation to various material and environment parameters and means of ablation testing.

The material classes of interest are:

1. Refractories and ceramics
2. Plastics
3. Elastomers
4. Composites.

Energy of decomposition, mass transfer blocking of convective heating, thermal diffusivity, and surface ablation temperature are some of the ablation parameters influencing the ablative material selection. Table 3 summarizes application of ablative materials and the general importance of selection criteria. The surface ablation temperatures are indicated to be high, moderate, or low as characteristic of efficient ablative materials for the application. The heating exposure time strongly influences insulative requirements.

The following paragraphs identify the sensitivity of ablation parameters to material properties, environmental effects, and thermostructural considerations.

4.1 Material Property Effects

Material properties have a broad influence on mass ablation (and surface recession) and on thermal insulative efficiency. The thermal insulation requirements are defined by the temperature which the structure and heat shield bond are capable of withstanding. Total weight requirements result from the anticipated mass loss and insulation demand.

The mass ablation comparisons in Figure 28 show that, although a carbonaceous material is more susceptible to oxidation, total mass loss is greater for the silica materials. The major reason is that surface ablation temperatures are greater for carbons, thus increasing surface reradiation and reducing the convective heating - also $\varepsilon_s = 0.9$ for carbon base materials and $\varepsilon_s = 0.5$ for silica base materials.

TABLE

ABLATIVE MATERIAL APPLICATIONS AND SELECTION CRITERIA

Application	Heating Exposure Time (Seconds)	Weight Per Unit Surface Area	Mass Ablation Rate	Thermal Insulative Properties	Surface Ablation Temperature	Surface Recession
1. High-Performance Conical Reentry Vehicles (w/c_DA > 1500 psf):	15 to 40					
a. Nosecap		Unimportant	Less Important	Unimportant	High	Important
b. Conical Section		Important	Important	Important	High	Less Important
c. Aft Cover		Important	Unimportant	Important	Low to Moderate	Unimportant
2. Low-Ballistic Coefficient Reentry Vehicles (w/c_DA < 1500 psf):	20 to 100					
a. Nosecap		Less Important	Important	Less Important	High	Important
b. Other Regions		Important	Important	Important	Moderate to High	Unimportant
c. Aft Cover		Important	Unimportant	Important	Low	Unimportant
3. Low to Intermediate Range Ballistic Missiles	10 to 50					
a. Nosecap		Less Important	Important	Less Important	Moderate to High	Less Important
b. Other Regions		Important	Important	Important	Low to Moderate	Unimportant
c. Aft Cover		Important	Unimportant	Important	Low	Unimportant
4. Lifting, Satellite and Planetary Entry	300 to 2000	Important	Unimportant	Important	Moderate	Important
5. Launch and Booster Insulation	5 to 200	Important	Unimportant	Important	Low	Unimportant
6. Rocket Nozzles	1 to 100					
a. Throat		Less Important	Unimportant	Less Important	High	Important
b. Other Regions		Important	Less Important	Important	High	Less Important
7. Hypersonic Interceptor Missiles	5 to 100					
a. Nosecap and Control Fin Leading Edges		Unimportant	Less Important	Less Important	High	Important
b. Control Fins Forward Surface Regions		Important	Important	Important	Moderate to High	Unimportant
c. Other Regions		Important	Less Important	Important	Low to Moderate	Unimportant

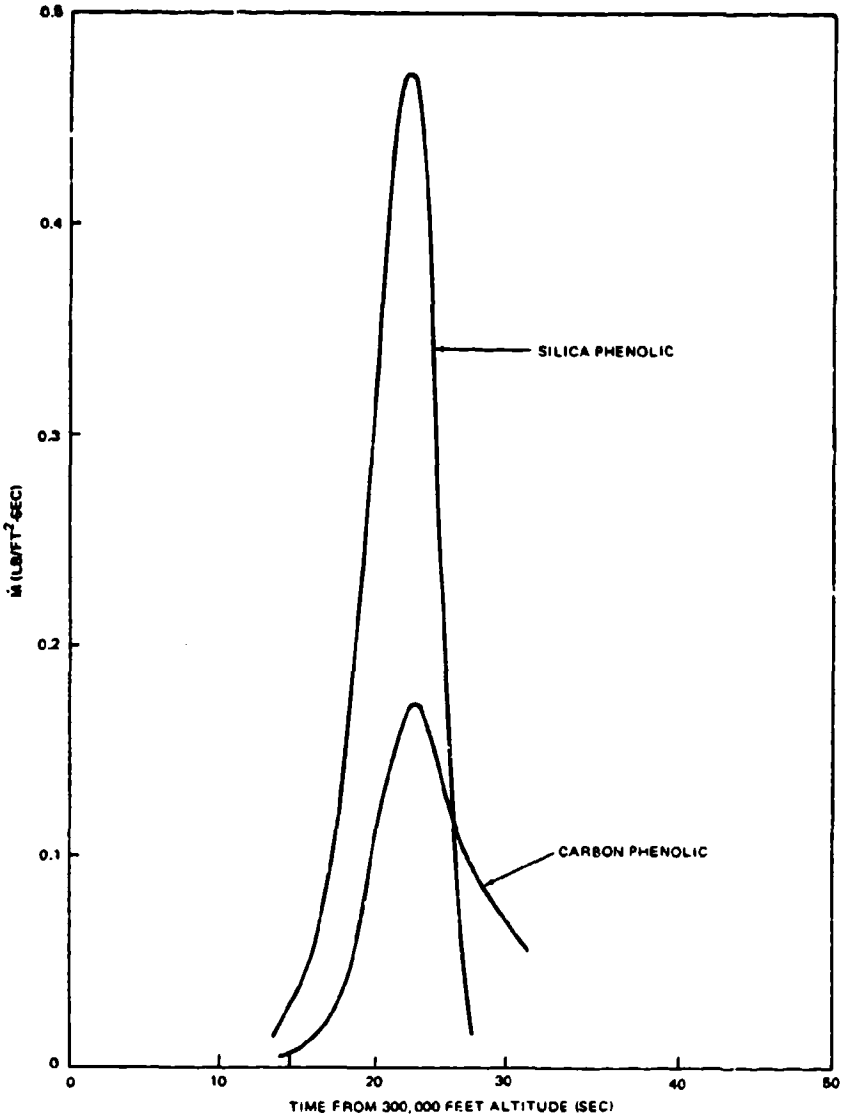

Comparison of Mass Ablation Rates Between Silica Phenolic and Carbon Phenolic

Figure 28

Mass ablation rates are enhanced by liquid flow ablation, spallation of the char layer, and mechanical removal of the char layer. Silica base materials are susceptible to liquid flow surface recession. However, it is only important for nosecap applications and other regions subjected to significant pressure and shear gradients. A detrimental characteristic of many charring ablators is low-char strength. The application of ablative materials, such as the epoxies and elastomerics, is consequently restricted to low-shear and low-pressure regions or to vehicles subjected to less severe heating environments. Shear or spallation of the char is also an important consideration to high strength charring ablators.

Mass ablation may not be critical for some applications. Ablative material selection is strongly sensitive to material properties which influence thermal insulative performance. A numerical description of the transient heat conduction relationship indicates the sensitivity to material properties with the dominant material property being the thermal conductivity since the specific heats for most ablative materials have nearly identical values.

Heat conducted into the ablative material is absorbed by pyrolysis decomposition and by the mass transfer toward the surface. The decreased density due to internal pyrolysis results in the thermal conductivity shifting from low-undecomposed material values to higher values for the char. An example of the influence of high-char thermal conductivity on phenolic-nylon ablation is shown in Figure 29. The thermal conductivity data are from (117). Although surface recession is low, the buildup of the char thickness near the end of flight is about 0.5 inch. The char density is about 0.30 times the original density of 72 lb/ft^3; consequently, internal mass transfer removed a significant fraction of heat conducted in at the surface.

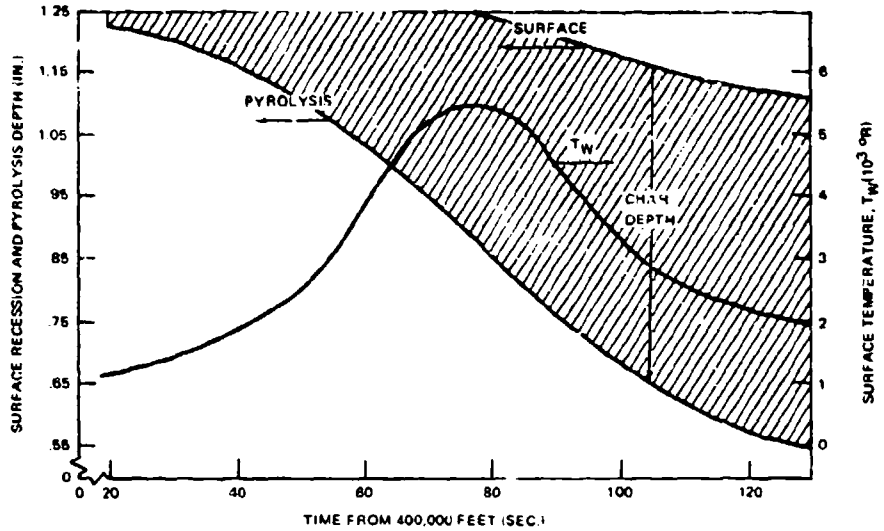

Figure 29. Surface-Recession, Pyrolysis-Depth, and Surface-Temperature Histories for Phenolic Nylon Ablation

The insulative performance of ablation materials is a strong function of thermal conductivity as seen in the above example and (118). The thermal conductivities of several ablation materials are presented in Figure 23 as functions of temperature. The experimental correlation for phenolic nylon (117) is compared with an unpublished correlation derived with a charring ablator computer program which was used to correlate experimental ablation data. The data shown in Figure 30 are representative of different classes of ablative materials. Tungsten represents the refractory metals, graphites represent a class of materials by themselves, boron nitride is a representative refractory ceramic, carbon phenolic is a high-temperature and char strength composite, and phenolic nylon is representative of the plastic composites. Purple blend MOD-5 is one of a class of materials specifically tailored to provide low-thermal conductivity. Hydrogen gas and air thermal conductivities are shown for comparison purposes.

For applications requiring good insulative properties coupled to long heating exposure time, namely, lifting reentry vehicles, ablative plastic or elastomeric composites have been developed with the following properties to give improved insulative and ablative performance: (a) surface oxidation resistance, (b) low density, (c) low-char density, (d) low-molecular weight pyrolysis products, (e) fiber reinforcement for char strength, and (f) spherical voids. Examples of these materials are purple blend MOD-5 and phenolic cork.

Pyrolysis decomposition predicted using the Arrhenius rate equation has limited effects on ablative material performance provided the decomposition temperature is adequately duplicated, i.e., from about 800°R to 1500°R.

For materials which form thick chars evidence of "cracking" of gaseous hydrocarbons has been found through observed increases in densities of chars near the ablating surface. The effect on the ablative material char is to increase its strength and at the same time to increase the char thermal conductivity. Char layer spallation can result from deposition causing decreases in char permeability and increases in internal pressure.

4.2 Environmental Effects

As indicated above, ablation performance is sensitive to environmental effects. An increase in the convective heating rate usually increases ablation rates. However, if there is, e.g., a proportionate increase in reradiative effects, the increase will not materialize. An example of this effect is an increase in heating caused by higher enthalpy. Such changes in heating increase the ablation efficiency of the materials (118), and therefore do not increase ablation rates observed.

One effect of boundary layer enthalpy potential on ablation efficiency is in combustion reactions, which can be accounted for (119) by

$$\bar{q}_c = \frac{K_{oe} h_c}{(I_r - h_{env,w})} \tag{53}$$

in the following relationship

$$(\rho v)_w = \frac{\dot{q}_{w_o}(1 + \bar{q}_c) - \dot{q}_r}{\eta(1 + \bar{q}_c)(I_r - h_{env,w}) + \Delta E} \tag{54}$$

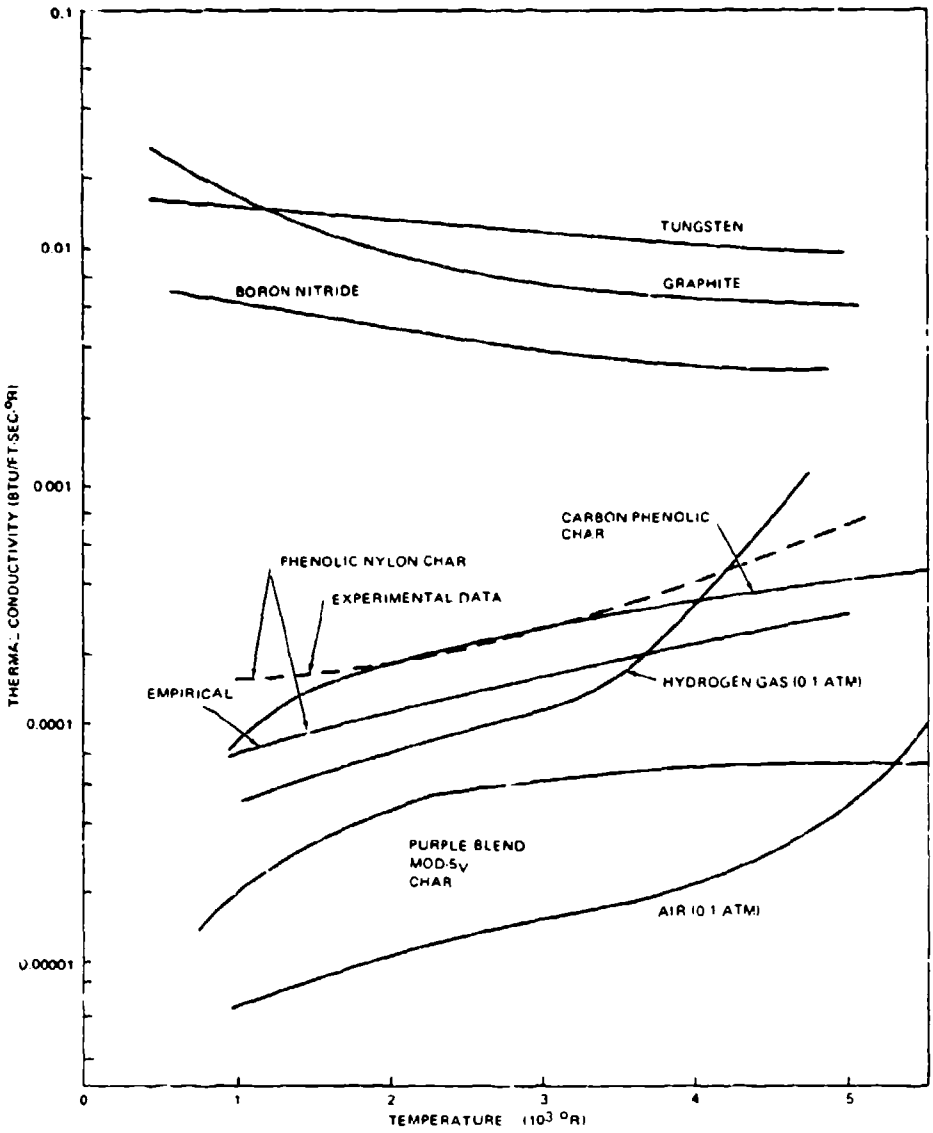

Figure 30. Comparisons of Thermal Conductivities

where

$$\Delta E = \frac{\dot{m}_{c_s}}{\dot{m}_v} H_v + \frac{\dot{m}_{c_s}}{\dot{m}_v} h_{c_s} + \frac{\dot{m}_{g_s}}{\dot{m}_v} h_{g_s}$$

h_c = heat in combustion per unit mass of oxygen

K_{oe} = mass fraction of oxygen at the outer edge of the boundary layer

The term $\bar{q}_c$ gives an upper bound on the effect of combustion by assuming the all oxygen diffusing toward the surface reacts with the material vapor. For silica base materials this is not true and in a rocket nozzle environmental oxygen may be fixed as carbon monoxide.

In Eq (53) the combustion contribution ($K_{oe}h_c$) to heating and to the mass transfer blocking is independent of the boundary layer enthalpy potential. Consequently, combustion heating reactions are proportionately less important for high enthalpy potential heating environments that reentry vehicles experience over major portions of their flight. The variation in material efficiency that results with an increased enthalpy is shown in (118).

Environmental pressure and shear forces strongly influence ablation performance for reentry vehicles and to a lesser extent for throats of rocket nozzles. The charring ablators are recognized to have char strengths considerably lower than the strength of the undecomposed materials. Consequently, those materials which form weak chars are restricted to application in low pressure and shear environments.

4.3 Testing

Ablation testing is the method by which the analytical models are verified, many material properties are determined, and candidate heat shield materials are screened and selected. Because of the importance of testing in providing preflight design verification and confidence, it is obviously desirable to perform these tests in an accurately simulated if not duplicated flight environment. For many reasons (primarily facility power requirements and model size limitations) this is usually impossible, and tests must be run under several types of partial flight simulation. These results can then be evaluated by means of previously proven mathematical ablation models, or by overlapping the tests in such a way that a coherent composite picture of the important phenomena can be constructed (12).

Ballistic and lifting entry vehicles, designed for various missions, experience a wide range of entry environments. Two convenient parameters for illustrating these environments, which depend on flight performance rather than on geometry, are total enthalpy and stagnation point pressure. Figure 31 is a plot of pressure-enthalpy with overlays of typical entry-vehicle trajectories and maps of approximate simulation facility performance. Two important conclusions may be immediately reached:

1. No one facility can duplicate a complete flight environment, although large portions of some lifting-body trajectories can be closely approximated.

2. High pressure and high-enthalpy effects cannot be duplicated simultaneously.

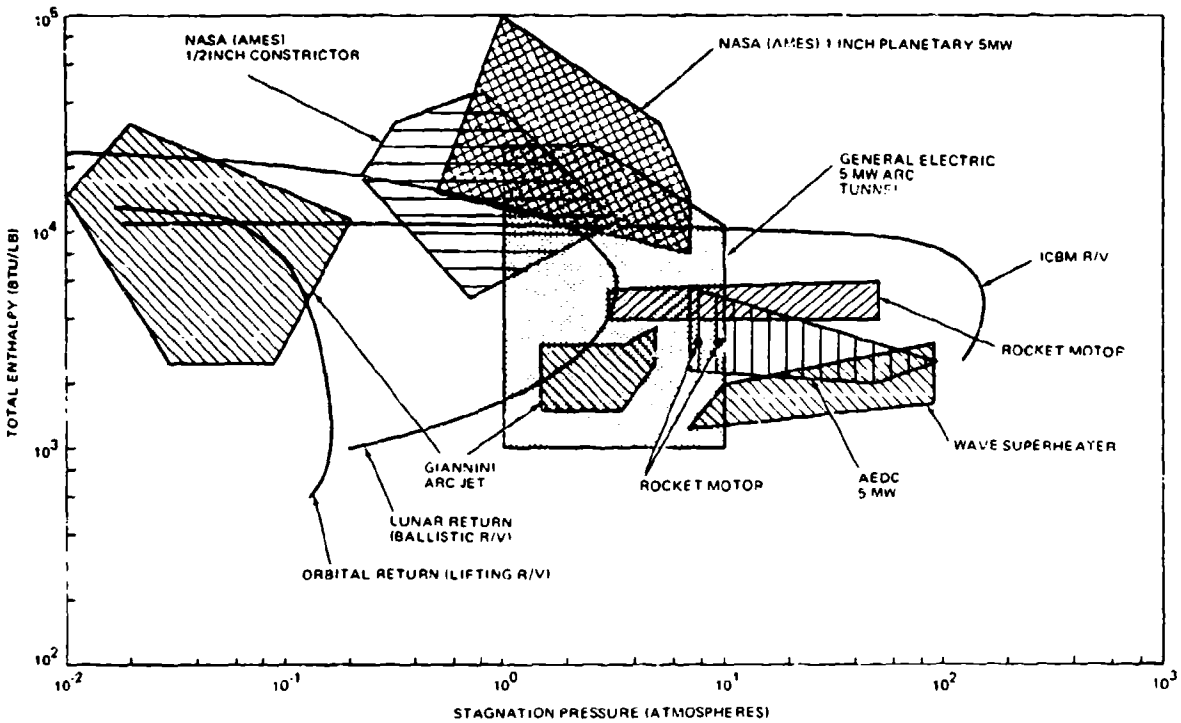

Figure 31. Comparison of Flight and Ablation Test Facility Performance Parameters

For simulation, steady state ablation is usually desired since this condition provides the necessary material parameters, evaluation for the analytical models. For this reason the facilities most applicable to entry ablation studies are the plasma-arc tunnel and the rocket-motor exhaust, both of which have operating times ranging from several seconds to several minutes. Facilities such as the ballistic range and shock tube are of only slight interest because of their very short test times -- approximately 10 milliseconds and 100 microseconds, respectively.

Because of simulation difficulties, test conditions must be carefully selected to obtain meaningful results. Plasma-arc facilities can frequently provide adequate simulation up to entry velocities of 30,000 ft/sec. The important simulation parameters for most ablation performance and screening tests are the heat flux and the enthalpy (121).

Efficient performance of the glassy ablators depends on the retention of the liquid melt layer, so the aerodynamic shear levels of flight should also be duplicated, if possible. The ablation performance of charring ablators is known to be reduced under very high pressures or pressure-gradients which tend to mechanically remove the char layer. For flight vehicles which will experience unusually high local pressures, such as low-drag ballistic entry vehicles, it may be necessary to simulate the pressure and shear levels as well as the heat flux and enthalpy. However, since this amounts to full scale flight duplication, these conditions must be simulated in separate tests and applied with much caution to the flight environments.

At the very high entry velocities which will be experienced in interplanetary return missions, the radiant heating from the shock-heated air can be equal to or significantly greater than the convective heating rates. Since the efficiency of most ablative materials depends on the heat blockage effect of the transpiring gases which will have little or no effect on the radiant heating, ablation performance will be reduced. Some plasma-arc facilities are available (122) which can superimpose radiant heating on the convective heating, and these must be employed for performance evaluation of materials to be used in this type of environment.

Because of the difficulties experienced in simulation of flight conditions in plasma arc facilities and variations in supposedly similar test conditions from facility to facility, several "round robin" test programs (123, 124, 125, 126) were conducted to compare the facilities and allow for a more meaningful comparison of test results. Also, several comparative material performance tests (126, 127) for some materials were conducted in a "round robin" fashion. As a result, better comparisons are available. Characteristics of various facilities are also given in the above references, as well as in (128, 129), and will not be tabulated again in this review. Due to the periodic changes in existing facilities range of performance, emergence of new facilities, and difficulty in obtaining up-to-date performance data, such tabulations do not retain permanent value.

REFERENCES

1. Hurwicz, H., et. al., "Thermal Protection Systems," ML-TDR-64-82, Air Force Materials Laboratory, Jan. 1965.

2. Munson, T. R. and R. J. Spindler, "Transient Thermal Behavior of Decomposing Materials, Part 1: General Theory and Application to Convective Heating," IAS Paper No. 62-30, presented at the 30th IAS Annual Meeting, New York, Jan. 1962.

3. Kratsch, K. M., L. F. Hearne, and R. R. McCheaney, "Thermal Performance of Heat Shield Composites During Planetary Entry," presented at the AIAA-NASA National Meeting, Palo Alto, Calif., Sept. 30 - Oct. 4, 1963.

4. Arne, C. L., "Ablative Materials Subject to Combustion and Thermal Radiation Phenomena," Douglas Paper No. 1851, Jan. 1964.

5. Kendall, R. M., R. A. Rindal, and E. P. Bartlett, "A Multicomponent Boundary Layer Chemically Coupled to an Ablating Surface," AIAA Journal, Vol. 5, No. 10, June 1967, pp. 1063-1071.

6. Adams, M. C., "Recent Advances in Ablation," J. Am. Rocket Soc. Vol. 29, No. 9, 1959, pp. 625-632.

7. Steg, L., "Materials for Re-entry Heat Protection of Satellites," J. Am. Rocket Soc. Vol. 30, Sept. 1960, p. 815.

8. Hurwicz, H., "Aerothermochemistry Studies in Ablation," printed from Combustion and Propulsion, (5th AGARDograph Colloquium) Pergamon Press, 1963, pp. 403-455.

9. Conference on Behavior of Plastics in Advanced Flight Vehicle Environments, compiled by H. S. Schwartz, WADD Technical Report 60-101, Sept. 1960.

10. Schmidt, D. L., "Ablation," Chapter 13, Engineering Design for Plastics, edited by Eric Baer, Reinhold Publishing Corp., 1964.

11. Minges, M. L., "Ablation Phenomenology - A Review," High Temperatures-High Pressures Journal, Vol. 1, No. 6, 1969.

12. Cordero, J., F. W. Diederich, and H. Hurwicz, "Aerothermodynamic Test Techniques for Re-Entry Structures and Materials," Aerospace Engineering, Vol. 22, No. 1, Jan. 1963, pp. 166-191.

13. Hurwicz, H. and J. E. Rogan, "Ablation," Section 16, to be published in the Handbook of Heat Transfer, edited by W. M. Rosenhow and J. P. Hartnett, McGraw Hill Book Company (in press).

14. Hurwicz, H. and J. E. Rogan, "High Temperature Thermal Protection Systems," Section 19, to be published in the Handbook of Heat Transfer, edited by W. M. Rosenhow and J. P. Hartnett, McGraw Hill Book Company (in press).

15. Dorrance, W. H., "Viscous Hypersonic Flow," McGraw Hill Book Company, 1962.

16. Sherman, M. M., "Entry Gasdynamic Heating," NASA SP 8XX, to be published.

17. Schmidt, D. L., "Ablative Polymers for Hypersonic Atmospheric Flight," AFML-TR 56-78, Air Force Materials Laboratory, May 1966.

18. Achard, R. T., "Fundamental Relationships for Ablation and Hyperthermal Heat Transfer, AFFDL-TR-66-25, April 1966.

19. Munson, T. R., R. E. Mascola, J. D. Brown, R. J. Spindler, and J. Mugerman, "An Advanced Analytical Program for Charring Ablators - Final Report Volume I," AVCO Space Systems Division Report AVSSD-0172-67-RR.

20. Katsikas, C. J., G. K. Castle, and J. S. Higgins, "Ablation Handbook-Entry Materials Data and Design," AFML 66-262, Air Force Materials Laboratory, Nov. 1966.

21. Taylor, A. O., "A Transient Reaction Kinetics Analysis of Ablation Through Aerodynamic Heating," General Dynamics Convair Report Number GDC-ERR-AN-1029, Dec. 1965.

22. Enkenhus, H. R., "The Effect of Variable Lewis Number on Heat Transfer in a Binary Gas," AIAA Journal, Vol. 2, No. 4, 1964.

23. Brown, J. D., and F. A. Shukis, "An Approximate Method for Design of Thermal Protection Systems," presented at the IAS 30th Annual Meeting, New York, N.Y., Jan. 1962.

24. Hidalgo, H., "Ablation of Glassy Material Around Blunt Bodies of Revolution," ARS Journal, Vol. 30, Sept. 1960, p. 806.

25. Lees, L., "Convective Heat Transfer with Mass Addition and Chemical Reactions," printed from Combustion and Propulsion (3rd AGARDograph Colloquium), Pergamon Press, New York, 1958.

26. Hillberg, L. H., "The Convective Heating and Ablation Program (CHAP)," Boeing Report No. D2-36402-1, May 31, 1966.

27. Mathieu, R. D., "Mechanical Spallation of Charring Ablators in Hyperthermal Environments," AIAA Journal, Sept. 1964.

28. Fleddermann, R. G. and H. Hurwicz, "Analysis of Transient Ablation and Heat Conduction Phenomena at a Vaporizing Surface," Chemical Engineering Symposium Series, Vol. 57, No. 32, p. 2; also AVCO RAD-TR-9(7)-60-9, Apr. 1960.

29. Zlotnick, M. and B. Nordquist, "Calculation of Transient Ablation," presented at International Heat Transfer Conference, Boulder, Colorado, Sept. 1961; also AVCO RAD-9-TM-60-83, Jan. 1961.

30. Hurwicz, H. and R. G. Fleddermann, "Computer Simulation of Transient Ablation and Heat Conduction Phenomena at a Vaporizing Surface," presented at the ARS Space Flight Report to the Nation, New York, Paper No. 2209-61, Oct. 1961; also AVCO RAD-TR-9(7)-60-9, Apr. 1960.

31. Spindler, R. J. and H. Hurwicz, "Transient Heat Flow in Translucent Non-Gray Ablating Materials," Proceedings of Ballistic Missiles and Space Technology Conference, Vol. II; Pergamon Press, 1961; also AVCO RAD-TR-9(7)-59-27, Oct. 1959.

32. Hurwicz, H., W. C. Broding and A. J. Hanawalt, "An Approach to Re-Entry Thermal Protection/System Development," presented at the Bumble Bee Conference, St. Louis, Missouri, Nov. 1963.

33. Arne, C. L. and D. N. Kopec, "Charring Ablator Multiphase Processes Computer Program," Douglas Report SM-49310, June 17, 1960.

34. Stroud, C. W., "A Study of the Chemical Reaction Zone in Charring Ablators During Thermal Degradation," Master of Science Thesis, Virginia Polytechnic Institute, Blacksburg, Virginia, Sept. 1965.

35. Scala, S. M. and L. M. Gilbert, "Thermal Degradation of a Char-Forming Plastic During Hypersonic Flight," ARS Journal, Vol. 32, No. 6, 1962, pp. 917-924.

36. Duninberre, G. M., "Numerical Methods for Transient Heat Flow," Transactions of the ASME, Nov. 1945. pp. 703-712.

37. Schneider, P. J., T. A. Dolton, and G. W. Reed, "Charlayer Structural Response in High-Performance Ballistic Re-Entry," AIAA Paper No. 66-424, June 1966.

38. Kendall, R. M., et. al., "An Analysis of the Coupled Chemically Reacting Boundary Layer and Charring Ablator," Aerotherm Final Report No. 65-7, 1966.

39. Barriault, R. J. and L. Yos, "Analysis of the Ablation of Plastic Heat Shields that Form a Charred Surface Layer," ARS Journal, Vol. 30, Sept. 1960, p. 823

40. Metzger, J. W., W. J. Engle, and N. S. Diaconis, "Oxidation and Sublimation of Graphite in Simulated Re-Entry Environments," AIAA Journal, Vol. 5, No. 3, Mar. 1967, pp. 451-460.

41. Moore, J. A. and M. Zlotnick, "Combustion of Carbon in an Air Stream," ARS Journal, Vol. 31, Oct. 1961, pp. 1388-1397.

42. Anon., "JANAF Thermodynamic Properties," Dow Chemical Company, Midland, Michigan.

43. Scala, S. M. and N. S. Diaconis, "The Stagnation Point Ablation of Teflon during Hypersonic Flight," Journal Aeronautical Science, Vol. 27, No. 2, 1960.

44. Welsch, W. E. and K. E. Starner, "Low Density Ablation Materials Survey," Air Force Ballistic Systems and Air Force Space Systems Division, Aerospace Corporation Report No. SSD-TR-66-35 TDR-669 (6240-10)-5., Jan. 1966.

45. Beecher, N. and R. E. Rosenweig, "Ablation Mechanisms in Plastics with Inorganic Reinforcement," ARS Journal, Vol. 31, Apr. 1961, p. 532.

46. Ladacki, M. J. V. Hamilton and S. H. Cobs, "Heat of Pyrolysis of Resin in Silica Phenolic Ablator," AIAA Journal, Vol. 4, No. 10, Oct. 1966, pp. 1798-1802.

47. Swann, R. T., C. M. Pitmann, and J. C. Smith, "One-Dimensional Numerical Analysis of the Transient Response at Thermal Protection Systems," NASA TN-D-2976, Sept. 1965.

48. Coleman, W. D., J. M. Lefferdo, L. F. Hearne, and H. S. Vojvodich, "A Study of the Effects of Environmental and Ablator, and Performance Uncertainties on Heat Shielding Requirements for Blunt and Slender Hyperbolic-Entry Vehicles, Paper 68-154, AIAA 6th Aerospace Sciences Meeting, Jan. 1968.

49. Ridgon, W. S., R. B. Dirling, Jr., and M. Thomas, "Radiative and Convective Heating During Atmospheric Entry," NASA contractor's report to be published. March 1967.

50. Bishop, W. M. and V. DiCristina, "A Prediction Technique for Ablative Material Performance under High Shear Re-Entry Conditions," AIAA Journal, Vol. 6, No. 1, Jan. 1968.

51. Bishop, W. M. and V. DiCristina, "The Combustion and Sublimation of Carbon at Elevated Temperatures," AIAA Paper 68-759, June 1968.

52. Scala, S. M. and L. M. Gilbert, AIAA Journal, Vol. 3, No. 1635, 1968.

53. Meyer, C. B. and R. A. Rindal, "Finite Difference Solution for the In-Depth Response of Charring Materials Considering Surface Chemical and Energy Balance," Aerotherm Corporation Final Report No. 66-7, Part II, Mar. 1967.

54. Anon., "High-Quality Ablation Experimental Results, Phase I," Aerospace Report TR-0066, Apr. 1970.

55. Smith, D. H., et. al., High Temperatures-High Pressures International Journal of Research - to be published.

56. Feldmann, S., "On the Instability Theory of the Soft Melted Surface on an Ablating Body when Entering the Atmosphere," AVCO Research Laboratory, Research Report No. 34, Aug. 1958.

57. Chapman, D. R., H. K. Larson, and L. A. Anderson, "Aerodynamic Evidence Pertaining to the Entry of Tektites into the Earth's Atmosphere," NASA TR-R-134, 1972.

58. Chapman, D. R. and H. K. Larson, "The Lunar Origin of Tektites," NASA TN D-1556, Feb. 1963.

59. Larson, H. K. and G. G. Mateer, "Cross-Hatching - A Coupling of Gas Dynamics with the Ablation Process," AIAA Paper 68-670, 1968.

60. Canning, T. N., M. E. Wilkins, and M. E. Tauber, "Boundary-Layer Phenomena Observed on the Ablated Surface of Cones Recovered after Flights at Speeds up to 7 Km/Sec," AGARD CP-19, Vol. 2, 1967.

61. Canning, T. N., M. E. Wilkins, and M. E. Tauber, "Ablation Patterns on Cones Having Laminar and Turbulent Flows," AIAA Journal, Vol. 6, No. 1, Jan. 1968, pp. 174-175.

62. Canning, T. N., M. E. Tauber, M. E. Wilkins, and G. T. Chapman, "Orderly Three-Dimensional Processes in Turbulent Boundary Layers on Ablating Bodies, AGARD, CP-30, 1968.

63. Laganelli, A. L. and D. E. Nestler, "Surface Ablation Patterns: A Phenomonology Study," AIAA Journal, Vol. 7, No. 7, July 1969, pp. 1319-1325.

64. Williams, E. P., "Experimental Studies of Ablation Surface Patterns and Resulting Roll Torques," AIAA Journal, Vol. 9, No. 7, July 1971, pp. 1315-1321.

65. Williams, E. P. and G. R. Inger, "Ablation Surface Cross-Hatching on Cones in Hypersonic Flow," AIAA Journal, Vol. 9, No. 10, Oct. 1971, pp. 2077-2078.

66. Stock, H. W. and J. J. Ginoux, "Experimental Results on Crosshatched Ablation Patterns." AIAA Journal, Vol. 9, No. 5, May 1971, pp. 971-973.

67. McDevitt, J. B., "An Exploratory Study of the Roll Behavior of Ablating Cones," Journal Spacecraft and Rockets, Vol. 8, No. 2, Feb. 1971, pp. 161-169.

68. Tobak, M., "Hypothesis for the Origin of Cross-Hatching," AIAA Journal, Vol. 8, No. 2, Feb. 1970, pp. 330-334.

69. Bachtsheim, P. R., "Analysis of the Stability of a Thin Liquid Film Layer Adjacent to a High Speed Gas Stream," NASA TN D-4976, 1969.

70. Gold, H., R. J. Probstein, and R. S. Scullen, "Inelastic Deformation and Crosshatching," AIAA Paper 70-768, Los Angeles, 1970.

71. Williams, E. P. and G. R. Inger, "Investigations of Ablation Surface Crosshatching," SAMSO TR70-246, USAF Space and Missile Systems Organization, Norton Air Force Base, California, June 1970.

72. Maahs, H. G. and D. R. Schryer, "Particle Removal in the Ablation of Artificial Graphite," AIAA Vol. 7, No. 11, Nov. 1969.

73. Lundell, J. H., et al., "Graphite ablation at Temperatures" AIAA Paper No. 71-418, April 26, 1971.

74. Whittaker, A. G. and P. Kinther, "Particle Emission During Sublimation of Graphite," Carbon Vol. 7, No. 3, June 1969, p. 414.

75. Mrozovski, S., "Mechanical Strength, Thermal Expansion and Structure of Cokes and Carbons," Proceedings of the First and Second Conference on Carbon, 1956.

76. Riley, W. C., "Graphite," High Temperature Materials and Technology, John Wiley and Sons, Inc., 1967.

77. Kratsch, K. M., et. al., "Graphite Ablation in High-Pressure Environments," presented at AIAA Entry Vehicle Systems and Technology Conference, Williamsburg, Virginia, Dec. 3 - 5, 1968.

78. McVey, D. F., I. Auerback, and D. D. McBride, "Some Observations on the Influence of Graphite Microstructure on Ablation Performance," presented to AIAA 8th Aerospace Sciences Meeting, New York, Jan. 19 - 21, 1970.

79. Denman, G. L. and M. L. Minges, "High Pressure Ablation of Plastic Composites and Graphites in the 50 Megawatt Arc," presented to AIAA 3rd Fluid and Plasma Dynamics Conference, Los Angeles, June 29 - July 1, 1970.

80. Stetson, K. F., "Boundary-Layer Transition on Blunt Bodies with Highly Cooled Boundary Layers," JAS, Vol. 27, No. 2, Feb. 1960, pp. 81-91.

81. McCauley, W. D., A. R. Saydah, and J. F. Bueche, "Effect of Spherical Roughness on Hypersonic Boundary-Layer Transition," AIAA Journal, Vol. 4, No. 12, Dec. 1966, pp. 2142-2148.

82. Cresci, R. J., C. A. MacKenzie, and P. A. Libby, "An Investigation of Laminar, Transitional, and Turbulent Heat Transfers on Blunt-Nosed Bodies in Hypersonic Flow," JAS, Vol. 27, No. 6, June 1960, pp. 401-414.

83. Bandettini, A. and W. E. Isler, "Boundary-Layer-Transition Measurements on Hemispheres of Various Surface Roughnesses in a Wind Tunnel at Mach Numbers from 2.48 to 3.55. NASA Memo 12-25-58A. Mar. 1959.

84. Braslow, A. L., S. C. Know, and E. A. Horton, "Effect of Distributed Three-Dimensional Roughness and Surface Cooling on Boundary-Layer Transition and Lateral Spread of Turbulence at Supersonic Speeds," NASA TN D-53, Oct. 1959.

85. Smith, A. M. O. and D. W. Clutter, "The Smallest Height of Roughness Capable of Affecting Boundary-Layer Transition in Low-Speed Flow," JAS, Vol. 26, 1959.

86. Peterson, J. B., and E. A. Horton, "An Investigation of the Effect of a Highly Favorable Pressure Gradient on Boundary-Layer Transition as Caused by Various Types of Roughnesses on a 10-Foot-Diameter Hemisphere at Subsonic Speeds," NASA Memo 2-58-59L, April 1959.

87. Holloway, P. F. and J. R. Sterrett, "Effect of Controlled Surface Roughness on Boundary-Layer Transition and Heat Transfer at Mach Numbers of 4.8 and 6.0," NASA TN D-2054, April 1964.

88. Klebanoff, P. S., G. B. Schubauer, and K. D. Tidstrom, "Measurements of the Effect of Two-Dimensional and Three-Dimensional Roughness Elements on Boundary-Layer Transition," JAS, Vol. 22, No. 11, Nov. 1955.

89. Stainback, C. P., "Some Effects of Roughness and Variable Entropy on Transition at a Mach Number of 8," AIAA Paper 67-132, Jan. 1967.

90. Carros, R. J., "Effect of Mach Number up to 7.4 on Boundary-Layer Transition in the Presence of Pressure Rise and Surface Roughness on an Ogive-Cylinder Body with Cold Wall Conditions," NACA RM A56B15, April 1956.

91. Bertram, M. H., L. M. Weinstein, and A. M. Cary, Jr., "Effect of Two-Dimensional Multiple-Wave Distortions on the Heat Transfer to a Wall in Hypersonic Flow," AIAA Paper No. 67-164, Jan. 1967.

92. Bertram, M. H. and M. M. Wiggs, "Effect of Surface Distortions on the Heat Transfer to a Wing at Hypersonic Speeds," IAS Paper No. 62-127, June 1962.

93. Cary, Jr., A. M., and E. E. Morrisette, "Effect of Two-Dimensional Multiple Line-Wave Protrusions on the Pressure and Heat Transfer Distribution for a Hot Plate at Mach 6," NASA TN D-4437, Mar. 1968.

94. Welsh, Jr., W. E., "Shape and Surface Roughness Effects on Turbulent Nose Tip Ablation," AIAA Paper No. 69-717, June 16-18, 1969.

95. Akin, C. M. and J. G. Marvin, "Anomalous Convective Stagnation Point Heat Transfer at High Pressure," Presented at the 29th Semiannual Meeting of the Supersonic Tunnel Association, Silver Spring, Maryland, April 22-23, 1968.

96. AVCO Systems Divisions, "Thermomechanical Erosion of Ablative Plastic Composites," Report AVSD-0095-70-CR, Jan. 1970.

97. Weil, N. A., (Ed), "Studies of the Brittle Fracture of Ceramic Materials," ASD-TR 61-628II. Spiral, 1963.

98. Shaffer, P. T. B., D. P. H. Hasselman, and A. Z. Chaberski, "Factors Affecting Thermal Shock Resistance of Polyphase Ceramic Bodies," WADD Technical Report 60-749, Part I, 1961, p. 57.

99. Greszczuk, L. B., "Elastic Constants and Analysis Methods for Filament Wound Shell Structures," Douglas Report SM-45849, McDonnell Douglas Astronautics Company - Western Division, Santa Monica, California, Jan. 1964.

100. Welsh, W. E. and P. M. Chung, "A Modified Theory for the Effect of Surface Temperature on the Combustion Rate of Carbon Surfaces in Air," Proceedings of the 1963 Heat Transfer and Fluid Mechanics Institute, Stanford University Press, June 1963.

101. Hearne, L. F., L. W. Gallagher, and L. W. Woodruff, "Surface Oxidation with Streamwise Variation of Wall Reactivity," AIAA 3rd Thermophysics Conference, Paper No. 68-755, Los Angeles, California, June 1968.

102. Pitzer, K. S., and E. Clementi, J. Am. Chem. Soc., Vol. 81, 1959, p. 4477.

103. Duff, R. E., and S. H. Bauer, J. Chem. Phys., Vol. 36, 1962, p. 1754.

104. Dolton, T. A., R. E. Maurer, and H. E. Goldstein, AIAA 3rd Thermophysics Conference, Paper No. 68-754, Los Angeles, California, June 1968.

105. Basset, J., Chemie and Industrie, Vol. 45, No. 3f, 1941, p. 7.

106. Scala, S. M. and L. M. Gilbert, "The Sublimation of Graphite at Hypersonic Speeds," General Electric Co. Missile and Space Division, R64SD55, Aug. 1964.

107. McChesney, H. R., "Sublimation Energy and Vapor Equation of State for Graphite," Lockheed Missiles and Space Co., Dec. 31, 1963.

108. Krieger, F. J., "Thermodynamics of the Graphite-Carbon Vapor System," The Rand Corp., RM 3326 PR, Sept. 1962.

109. Baun, W. L. and D. W. Fisher, J. Chem. Phys., 35, 1961, p. 1518.

110. Dörnenburg, E., H. Hintenberger, and J. Franzen, Z. Naturfursch, Vol. 16a, 1961, p. 532.

111. Hoffmann, R., J. Chem. Phys., Vol. 39, 1963, p. 1397.

112. Drowart, J., R. P. Burns, G. DeMaria, and M. G. Inghram, J. Chem. Phys., Vol. 31, 1959, p. 1131.

113. Thorn, R. J., and G. H. Winslow, J. Chem. Phys., Vol. 26, 1957, p. 186.

114. Schoessow, G. J., "Graphite Triple Point and Solidus-Liquidus Interface Experimentally Determined up to 1000 Atmospheres," College of Engineering, University of Florida, Dec. 1967.

115. Fateeva, N. I. et al., Doklady Akademie Nauk SSSR, Vol. 152, No. 1, 1963.

116. Rinehart, W. A., et. al., "High Impact Pressure (HIP) Arc Heater Facility," MDRL Report 71-14, McDonnell Douglas Research Laboratory, St. Louis, Apr. 1971.

117. Wilson, R. G., "Thermophysical Properties of Six Charring Ablators from 140° to 700°K, and Two Chars from 800° to 3000°K," NASA TN D-2991, Oct. 1965.

118. Swann, R. T., M. B. Dow and S. S. Tomkins, "Analysis of the Effects of Environmental Conditions on the Performance of Charring Ablators," AIAA Publication CY-9, AIAA Entry Technology Conference, Williamsburg & Hampton, Virginia, Oct. 12-14, 1964.

119. Hartnett, J. P. and E. R. G. Eckert, "Mass Transfer Cooling with Combustion in a Laminar Boundary Layer," Proceedings of the 1958 Heat Transfer and Fluid Mechanics Institute, University of California, Berkeley, June 1958.

120. Sherman, M. M., "Entry Thermal Protection," NASA SP-8014, Aug. 1968.

121. Georgiev, S., "The Relative Merits of Various Test Facilities with Regard to Simulation of Hypersonic Ablation Phenomena," Proceedings of the National Symposium on Hypervelocity Techniques, Denver, Colorado, IAS, Oct. 1960, pp. 162-174.

122. Anon., "Hyperthermal Test Facility," Giannini Scientific Corp., Santa Ana Division, Bulletin 15-009, June 1965.

123. Hiester, N. K. and C. F. Clark, "Relative Operating Capabilities of Selected Electric-Arc Reentry Environment Simulators, NASA CR-99, Sept. 1964.

124. Fisher, E. D., "Free Jet Flow Calibration Tests Conducted on the CAL Wave Superheater Test Facility and the APL High Pressure Arc Jet," Cornell Aeronautical Laboratory, New York, Dec. 29, 1966.

125. Fisher, E. D., "Free Jet Calibration Tests Conducted on the AEDC 5-Megawatt Arc Heater Test Unit," Cornell Aeronautical Laboratory, New York, May 23, 1966.

126. Fisher, E. D., "High Quality Ablation Program," SAMSO-TR-69-200, USAF Space and Missile Systems Organization, Norton Air Force Base, California, Nov. 1969.

127. Hiester, N. K. and C. F. Clark, "Comparative Evaluation of Ablating Materials in Arc Plasma Jets, NASA CR-1207, Dec. 1968.

128. Tillian, D. J., "Plasma Arc Facilities in the United States," LTV Report No. 0-7100/3R-22, Nov. 1963.

129. Rindal, R. A., "An Evaluation of Design Analysis Techniques for High Performance Ballistic Vehicle Graphite Nose Tips, Appendix D, Thermochemical and Thermomechanical Ablation," AFML TR-69-73, Vol. IV, Air Force Materials Laboratory, Jan. 1970.